ACS NANO

www.acsnano.org

REVIEW

Morphotaxy of Layered van der Waals Materials

David Lam, Dmitry Lebedev, and Mark C. Hersam*

Cite This: *ACS Nano* 2022, 16, 7144–7167

Read Online

ACCESS | Metrics & More | Article Recommendations

ABSTRACT: Layered van der Waals (vdW) materials have attracted significant attention due to their materials properties that can enhance diverse applications including next-generation computing, biomedical devices, and energy conversion and storage technologies. This class of materials is typically studied in the two-dimensional (2D) limit by growing them directly on bulk substrates or exfoliating them from parent layered crystals to obtain single or few layers that preserve the original bonding. However, these vdW materials can also function as a platform for obtaining additional phases of matter at the nanoscale. Here, we introduce and review a synthesis paradigm, *morphotaxy*, where low-dimensional materials are realized by using the *shape* of an initial nanoscale precursor to template growth or chemical conversion. Using morphotaxy, diverse non-vdW materials such as HfO_2 or InF_3 can be synthesized in ultrathin form by changing the composition but preserving the shape of the original 2D layered material. Morphotaxy can also enable diverse atomically precise heterojunctions and other exotic structures such as Janus materials. Using this morphotaxial approach, the family of low-dimensional materials can be substantially expanded, thus creating vast possibilities for future fundamental studies and applied technologies.

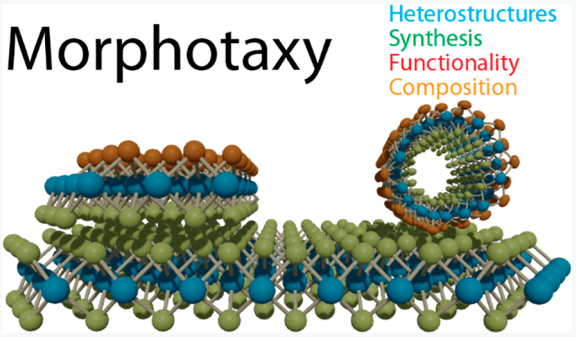

KEYWORDS: *two-dimensional materials, low-dimensional materials, synthesis, chemical conversion, oxidation, anionic modifications, cationic substitutions, heterostructures, Janus structures*

With the isolation of a single layer of graphene from layered graphite, Novoselov and Geim initiated the field of two-dimensional (2D) van der Waals (vdW) materials,[1] resulting in concentrated efforts to grow or exfoliate layered materials toward the atomically thin limit. Valued for their high aspect ratios, ease of gate tunability, and size-dependent properties, control over the composition and thickness of 2D materials has motivated synthetic efforts. The synthesis of 2D materials has largely focused on two strategies: a top-down approach that focuses on exfoliating naturally occurring layered crystals down to a single layer or a few layers and a bottom-up approach where growth occurs on bulk substrates starting from atomic or molecular precursors. The top-down approach aims to exfoliate individual, atomically thin sheets from a parent vdW crystal. Mechanical exfoliation, colloquially referred to as scotch-tape exfoliation, has been widely employed for the isolation of vdW monolayer flakes including graphene,[1] molybdenum disulfide,[2] and indium monoselenide[3] to name a few examples. While excellent at obtaining pristine, high-quality nanosheets for fundamental studies, mechanical exfoliation is not a scalable process and results in an inhomogeneous distribution of nanosheets on a substrate.

Solution-based exfoliation is another top-down approach that offers a scalable alternative to mechanical exfoliation, which often comes at the cost of reduced quality of the resulting nanosheets.[4] The most prevalent solution-based technique, liquid-phase exfoliation (LPE), utilizes ultrasonication, shear mixing, or related agitation methods to delaminate layered crystals in appropriately chosen solvents, often with the addition of surfactants or other additives that aid exfoliation. LPE has been successfully applied to a wide variety of layered materials including graphene,[5] transitional metal dichalcogenides (TMDCs),[6] hexagonal boron nitride (hBN),[6] black phosphorus,[7] and germanium sulfide.[8] More sophisticated solution-based exfoliation protocols involve etching away

Received: January 8, 2022
Accepted: April 29, 2022
Published: May 6, 2022

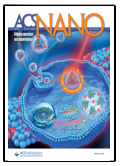

https://doi.org/10.1021/acsnano.2c00243
ACS Nano 2022, 16, 7144–7167

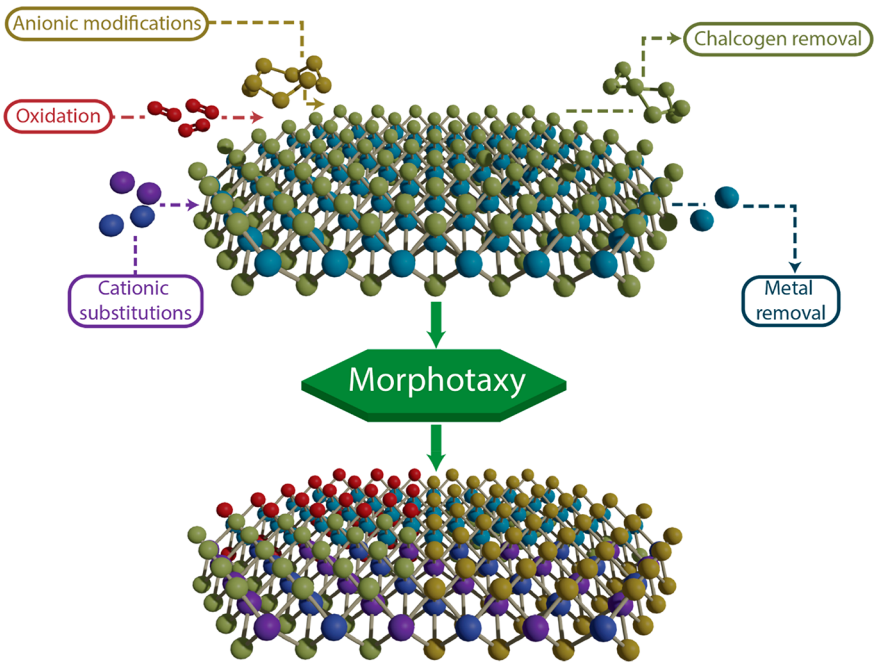

Figure 1. Avenues for morphotaxial synthesis. Oxidation-based modifications are useful for the formation of high-κ dielectrics, layer-by-layer thinning, and passivation. More generally, anionic modifications seek to remove or exchange chalcogens or other anionic species to form both layered and nonlayered 2D materials. While cationic substitutions are more difficult to accomplish than anionic modifications, emerging work with copper and related cations suggest significant opportunities in this direction. The end result in these morphotaxial pathways is a chemically distinct material that adopts the shape of the parent layered material.

metal atoms in a layered MAX structure (M = transition metal, A = group IIIA or IV element, X = carbon or nitrogen) to obtain 2D MXenes,[9−11] or introducing an intercalated ion, such as lithium[12] or tetrahexylammonium,[13] into the interlayer spacing of vdW materials prior to ultrasonication. These solution-based approaches are amenable to postexfoliation size selection using techniques such as liquid cascade centrifugation[14] or density gradient ultracentrifugation.[15] After size sorting, LPE 2D materials can be assembled on substrates using a diverse set of additive manufacturing methods such as layer-by-layer assembly,[16,17] inkjet printing,[18] and screen printing.[19] Despite the many advantages provided by the scalable nature of solution-based exfoliation, the resulting flakes often possess higher defect densities and compromised properties compared to mechanical exfoliation. Moreover, both mechanical and solution-based exfoliation rely on having a high-quality, layered parent crystal, which constrains the number of different 2D materials that can be derived using the top-down methodology.

Bottom-up approaches, in contrast, seek to synthesize single to few layer materials from atomic or molecular precursors, instead of relying on layered parent crystals. Bottom-up synthesis can be performed in solution,[4] which has been utilized to prepare colloidal solutions of TMDCs,[20] tailor defect density in MoS_2 for hydrogen evolution reactions,[21] and even synthesize ambient-reactive 2D materials such as CrI_3.[22] While solution-phase synthesis offers high levels of synthetic tunability, it generally results in highly defective 2D materials and relies on stabilizing ligands that can compromise materials properties. Vapor deposition has also been employed as an alternative bottom-up synthetic approach. For example, chemical vapor deposition (CVD)[23,24] has been shown to grow large-area films by relying on van der Waals epitaxy to nucleate layered materials such as MoS_2[25,26] and Bi_2O_2Se.[27−29] CVD growth often yields electronic-grade 2D materials that have been used in next-generation electronic devices such as MoS_2 transistors[30] and photodetectors.[31] In addition, CVD growth allows achieving monolayers with control over the density of defects and in particular grain boundaries, which was used for fabrication of memristors[25] and memtransistors.[26] Closely related to CVD are other vapor deposition schemes such as pulsed-laser deposition[32] for InSe[33] and physical vapor deposition[34] for elemental 2D materials[35,36] that rely on the vaporization and subsequent condensation of the material onto a target substrate. One advantage of vapor deposition schemes is that they enable the growth of entirely synthetic 2D materials that are not layered in the bulk.[37] However, vapor deposition methods are energy intensive and often yield films with small grain sizes. Furthermore, the outcome of vapor deposition is typically substrate-dependent, which then necessitates the development of transfer schemes to utilize the resulting 2D material in arbitrary device geometries. Finally, molecular beam epitaxy (MBE) is another class of bottom-up synthesis that relies on the slow sublimation of material in an ultrahigh vacuum on a suitable substrate that allows the film to grow epitaxially.[38,39] MBE is even more sensitive than vapor deposition schemes in the control over the flux and suitability of substrates for epitaxial growth, resulting in comparatively higher costs.

While both top-down and bottom-up synthesis methods offer clear advantages in many contexts and have facilitated the rapid evolution of the 2D material field, previous reports have been primarily constrained by the choice of one synthetic avenue. Instead, combining elements of multiple synthetic routes has the potential to achieve compositions and morphologies that are not achievable with only one top-down or bottom-up approach. For example, performing a bottom-up chemical reaction on a 2D material isolated using a

https://doi.org/10.1021/acsnano.2c00243
ACS Nano 2022, 16, 7144−7167

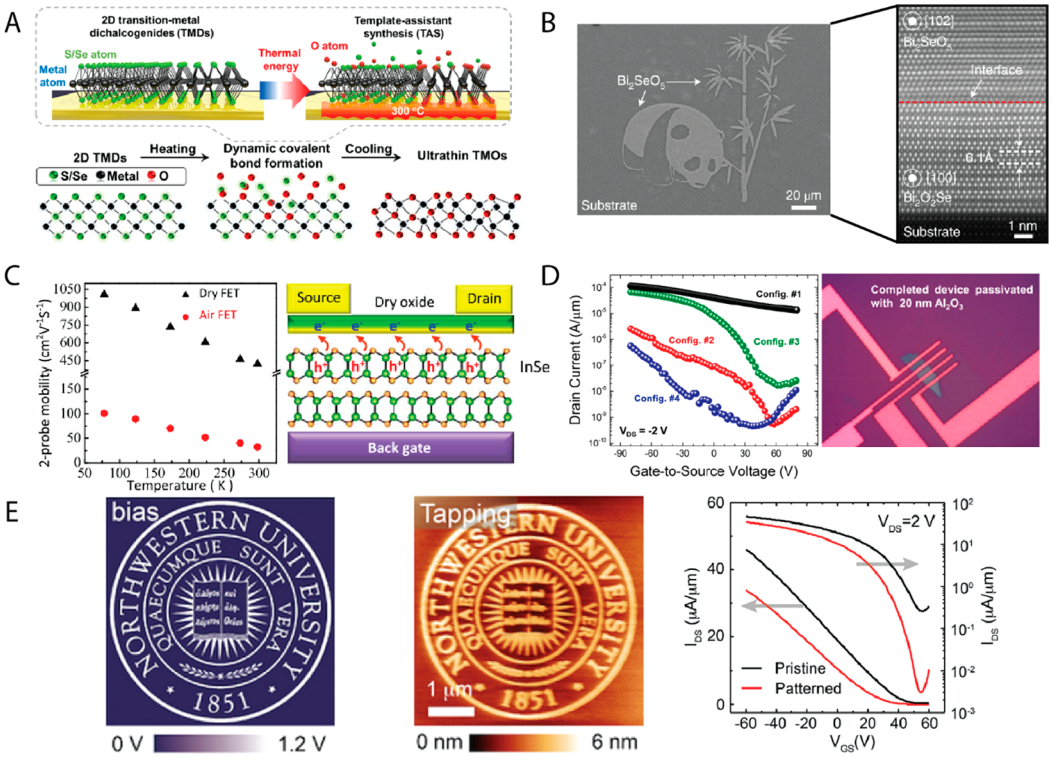

Figure 2. Oxidation-based morphotaxy. (A) Schematic for the synthesis of transition metal oxides (TMOs) *via* template-assisted synthesis. Thermally activated oxygen annealing results in the chalcogens in 2D TMDCs being replaced by oxygen atoms, thus forming amorphous ultrathin TMOs that retain the shape of the parent nanosheet. Reproduced with permission from ref 44. Copyright 2016 American Chemical Society. (B) Bi_2SeO_5, a high-κ dielectric, is formed on top of a Bi_2SeO_2 film. By use of electron-beam lithography (EBL), the native oxide can be patterned and forms an atomically sharp interface with the underlying semiconducting Bi_2SeO_2. Reproduced with permission from ref 51. Copyright 2020 Springer Nature. (C) Formation of a dry native oxide on InSe transistors provides passivation and results in higher field-effect transistor (FET) mobilities than pristine devices. Reproduced with permission from ref 68. Copyright 2017 American Chemical Society. (D) Black phosphorus (BP) can be thinned *via* repeated oxidation and vacuum annealing. With use of an Al_2O_3 mask and EBL to define features, a FET is fabricated on top of a BP flake with two different thicknesses (11.7 and 8.7 nm). The transfer curves demonstrate that in the case of BP heterojunctions (configurations 3 and 4), the on/off ratio is enhanced compared to those of thick BP (configuration 1) and thin BP (configuration 2). Reproduced with permission from ref 81. Copyright 2017 American Chemical Society. (E) Scanning probe thinning of BP. Applying a DC bias in a patterned fashion results in sub-micrometer features that are readily rinsed away with water to form thinned regions of BP. The FET on/off ratio increases to 10^4 from an initial value of 200 after the scanning probe patterning reduces the thickness of the BP nanosheet. Reproduced with permission from ref 82. Copyright 2016 Wiley. Permission to use the Northwestern University logo was confirmed by Mark C. Hersam.

top-down approach can enable non-vdW heterostructures, passivation of ambient-reactive 2D materials, or doping of atomically thin materials. In this Review, we refer to this combined synthetic paradigm as *morphotaxy*, after the Greek prefix for shape (*morpho-*). Morphotaxy seeks to utilize the *shape* of an initial nanoscale precursor to direct the growth of low-dimensional materials (Figure 1). In contrast to existing synthetic schemes, morphotaxy takes advantage of already existing layered or ultrathin materials to initiate reactions, resulting in a product that bears the same shape as the parent crystal. While similar in concept to epitaxy, where single-crystal materials are grown on top of a lattice-matched substrate, or topotaxy, where the end product has its crystallographic direction determined by the growth precursor,[40] morphotaxy focuses on determining the shape of the final low-dimensional material, allowing for reactions that may change the crystalline structure or result in amorphous materials that are nevertheless atomically thin and smooth. For example, through morphotaxial reactions, one can achieve encapsulation with ultrathin and smooth oxides, modulate surface states, or form atomically precise heterostructures on the same nanosheet.[41] Moreover, morphotaxy enables the synthesis of non-vdW 2D compounds by directing reactions constrained by the original crystal shape, in addition to Janus structures that break symmetry due to complete conversion of only one side of a layered material.

In this Review, we examine the current literature on 2D materials synthesis through a morphotaxial lens. The first section focuses on oxidation-based modification, which is arguably the most studied example of morphotaxy and illustrates the versatility of morphotaxy in enabling complex patterning and functionality in electronic devices. The second section highlights anionic modifications with an extensive discussion of chalcogenide morphotaxy in addition to rarer cases such as the carburization, nitridation, and fluorination of ultrathin metals or layered materials. The third section considers the relatively understudied case of cationic modifications with a particular focus on copper-based morphotaxy. Following this comprehensive survey of the current literature, we conclude by providing a forward-looking perspective on the future of morphotaxy, outlining possible research directions that have the potential to dramatically expand the number of synthetically achievable low-dimensional materials.

https://doi.org/10.1021/acsnano.2c00243
ACS Nano 2022, 16, 7144−7167

OXIDATION-BASED MORPHOTAXY

Oxidation-based modifications represent the most studied form of morphotaxy with rich applications ranging from high-κ dielectrics to passivation of reactive surfaces. The versatility and relative ease of driving oxidation-based reactions also lends itself to complex patterning schemes that take full advantage of morphotaxial principles in creating complex structures of layered materials.

High-κ Dielectric Morphotaxy. Electronic devices utilizing 2D materials as the semiconducting channel in a field-effect transistor (FET) geometry often suffer from low mobilities, poor subthreshold voltage swings, and time-dependent degradation of key parameters (*e.g.*, threshold voltage). These issues can at least partially be traced to poor interfaces between the gate insulator and the channel material. Unlike in the case of silicon-based technology, amorphous oxide growth on 2D vdW materials is hindered by the lack of dangling bonds on the surface that traditionally nucleate growth.[42,43] On the other hand, 2D insulators such as hBN provide a well-defined interface and a low density of dangling bonds and trap states at the interface that yield improved mobilities and subthreshold swings but suffer from low dielectric constants, narrow bandgaps, or both.[41] Consequently, the realization of high-κ atomically flat oxides with low density of dangling bonds grown directly on 2D semiconductors with a van der Waals interface is of immense technological interest for electronic applications.

Using a technique called template-assisted synthesis, Cui *et al.* have synthesized amorphous, ultrathin transition metal oxides (TMOs) by annealing metallic TMDCs such as TiS_2, TaS_2, and $TaSe_2$ in oxidizing environments at 300 °C.[44] The authors showed the exchange of oxygen with sulfur and selenium atoms, resulting in TMOs that retained the shape of the parent crystal (Figure 2A). Following oxidation, the surface roughness of the resulting TiO_2 and Ta_2O_5 was less than 0.3 nm, demonstrating that atomically flat surfaces are retained. Subsequent capacitance–voltage measurements utilizing the TMOs as the insulator in a metal–insulator–metal diode structure revealed that the dielectric constant of TiO_2 synthesized in this fashion is ∼18, which is consistent with the literature on amorphous TiO_2.[44] Chamlagain *et al.* built upon this result to fabricate a MoS_2 FET with thermally oxidized TaS_2 as the high-κ dielectric.[45] In this case, the authors reported a MoS_2 device with a Ta_2O_5 top gate dielectric (channel length ∼2 μm) formed through template-assisted synthesis that exhibited a subthreshold swing of 61 mV dec^{-1} and an on/off ratio approaching 10^6 with a field-effect mobility of 61.5 $cm^2\ V^{-1}\ s^{-1}$.[45] These results confirm the viability of morphotaxially converting TMDC crystals into atomically smooth dielectrics with a clean dielectric–channel interface that can be effectively utilized in 2D semiconductor electronic devices.

In addition to fully converting TMDCs into TMOs, related work has focused on partial morphotaxial conversion to yield oxide films on TMDCs. For example, Mleczko *et al.* formed high-κ native HfO_2 and ZrO_2 on $HfSe_2$ and $ZrSe_2$, respectively, *via* air exposure.[46] They also reported control over the native oxide thickness by controlling ambient exposure time, resulting in a high-κ oxide directly on these vdW materials.[46] Lai *et al.* similarly showed that 2D HfS_2 can be oxidized to high-κ HfO_2 with layer-by-layer control by tuning the reaction time with an oxygen plasma. A top-gated FET formed from the resulting HfO_2–HfS_2 heterostructure possessed a low interface trap density of $6 \times 10^{11}\ cm^{-2}\ eV^{-1}$ and an on/off ratio exceeding 10^7.[47] Peimyoo *et al.* instead used laser illumination to photo-oxidize HfS_2 that was pretransferred onto an existing 2D material stack, resulting in charge transfer between the semiconductor and trace amounts of adsorbed water to form HfO_2.[48] This approach allows for selective oxidation and patterning of the transferred material, even when sandwiched between 2D materials. A MoS_2 dual-gated FET utilizing 7 nm HfO_x synthesized in the aforementioned fashion as the top gate dielectric and SiO_2 as the bottom gate dielectric showed a threshold voltage of −0.4 V, an on/off ratio of $\sim 10^4$, and a subthreshold swing of ∼100 mV dec^{-1} with minimal hysteresis, which was attributed to the high-quality of the photo-oxidized dielectric.[48] The oxidation of TMDCs, in particular Hf-based and Ta-based dichalcogenides, thus provides a viable path for synthesizing ultrathin, atomically smooth, high-κ dielectrics.

While TMDCs are the natural start for exploring morphotaxial growth of dielectrics, semiconducting TMDCs suffer from lower mobilities than more recently discovered 2D semiconductors.[49] One such material, bismuth oxyselenide (Bi_2O_2Se), is of high interest due to its high mobility (150–450 $cm^2\ V^{-1}\ s^{-1}$ at room temperature) and moderate band gap (∼0.8 eV) that is suitable for telecommunications applications in addition to having a related dielectric oxide (bismuth selenite Bi_2SeO_5) with a high dielectric constant ($\kappa \approx 21$).[50] Li *et al.* synthesized bismuth selenite directly on the semiconducting channel by calcining Bi_2O_2Se at 370–400 °C.[51] This morphotaxial procedure formed Bi_2SeO_5 on top of Bi_2O_2Se with an atomically sharp interface as shown by cross-sectional high-angle annular dark-field scanning transmission electron microscopy (Figure 2B).[51] Furthermore, Bi_2SeO_5 can be selectively etched with dilute 0.2% HF acid, enabling complex patterns *via* electron-beam lithography (EBL) (Figure 2B). Using 5 nm thick Bi_2SeO_5 as the top gate oxide, Bi_2O_2Se-based FETs showed room-temperature on/off ratios of $\sim 10^5$ and mobilities of ∼250 $cm^2\ V^{-1}\ s^{-1}$.[51] Bi_2O_2Se nanoplates can also be selectively oxidized through an EBL-patterned polymer mask at room temperature using an oxygen plasma, as reported by Tu *et al.*[52] FETs with a ∼6 nm thick channel (Bi_2O_2Se) and ∼5 nm thick gate oxide (Bi_2SeO_x) resulted in room-temperature on/off ratios of $\sim 4 \times 10^4$ and mobilities of 60 $cm^2\ V^{-1}\ s^{-1}$.[52] These results demonstrate multiple avenues for morphotaxially forming dielectric oxides directly on high-performance layered semiconductors that are likely to inspire further research on other layered semiconductors with high-κ native oxides.

Other Applications for Oxide Morphotaxy. Morphotaxial oxide growth on vdW materials can also be beneficial in forming heterostructures, thinning multilayer crystals down to a desired thickness, passivating chemically reactive 2D materials, or tuning materials properties. This section will first discuss vertical heterostructures of TMDCs and TMOs for doping and thickness control, before moving onto analogous lateral heterostructures. Then, an overview on emerging work on ambient-reactive layered materials (termed post-TMDCs) will demonstrate that the reactivity of these layered materials can be a benefit, rather than a detriment, in facilitating morphotaxial reactions. Finally, a review of fundamental studies on oxidation will provide a roadmap for taking advantage of the rich opportunities offered by oxidation-based morphotaxy.

https://doi.org/10.1021/acsnano.2c00243
ACS Nano 2022, 16, 7144–7167

Vertical Heterostructures and Layer Thinning of TMDCs. Vertical heterostructures are not only limited to high-κ dielectric applications as discussed in the previous section but also enable other functionalities such as layer-specific thinning of 2D materials. Since many properties of TMDCs depend on thickness, it is critical to have fine control over the number of layers. As shown by Li *et al.*, low-power, remote oxygen plasma treatment of WSe_2 nanosheets resulted in only the top layer of WSe_2 being oxidized, with the layers below the oxide remaining pristine even following prolonged oxygen plasma treatments.[53] This observation was corroborated by Raman and photoluminescence (PL) spectroscopy as well as atomic force microscopy (AFM). The oxide layer can then be dissolved through a facile KOH treatment, enabling layer-by-layer etching of WSe_2.[53] Similarly, Pei *et al.* demonstrated analogous oxidation and layer-thinning in MoS_2 and WSe_2 through a direct oxygen plasma treatment.[54] At low powers, the oxygen plasma leads to first an oxidized monolayer on pristine MoS_2 and then subsequent removal of the oxide with longer treatment times. The authors noted that after oxide formation, the stability of the oxide under etching conditions plays a large role in further oxidation with the lower melting point of MoO_3 leading to more facile removal through the plasma treatment compared to the higher melting point WO_3.[54] This difference between the two materials suggests that more work is necessary to map out the phase space of oxygen plasma treatment time, intensity, and composition of the treated material in order to fully control oxidation and layer thinning *via* plasma treatments alone.

In addition to thickness control, morphotaxial oxidation can also be utilized to dope or provide improved electrical contacts for TMDCs. For instance, Ko *et al.* demonstrated MoO_3 growth on MoS_2 using an oxygen plasma treatment with the resulting MoO_3 overlayer forming in a layer-by-layer fashion that retains the atomic flatness of the parent MoS_2 flake.[55] Interestingly, unlike Pei *et al.*,[54] the authors do not report MoO_3 removal following extended plasma treatments, further emphasizing that the detailed processing conditions play a large role in the reaction outcome. Nevertheless, in this case, morphotaxial oxidation introduces hole doping or hole transport layers for MoS_2-based devices. For W-based TMDCs, Yamamoto *et al.* reported that a single, self-limiting WO_x layer formed on top of WS_2 flakes following ozone exposure, where the WO_x layer served as a p-type, quasi-Ohmic contact.[56] The WO_x was then further tuned by exposure to air and room-temperature ozone treatments, resulting in controllable hole doping and low Schottky barrier hole injection in atomically thin WSe_2 transistors with superlative room-temperature on/off ratios of $>10^7$ and hole mobilities of ~50 $cm^2\ V^{-1}\ s^{-1}$.[56] The same authors extended this result to show that morphotaxially grown WO_x can also serve as effective electron traps upon illumination, resulting in p-type photogating.[57] Specifically, using a WO_x-covered WSe_2 transistor, the authors observed a photoresponsivity of 3663 A/W at 1.1 nW, albeit with a slow response time on the order of seconds.[57]

Morphotaxial TMOs have also been shown to modulate the properties of additional 2D materials, resulting in devices such as tunable photodetectors and artificial synaptic devices. As shown by Ghasemi *et al.*, morphotaxial oxidation tuned the photoresponsivity of TiS_3 nanoribbon-based photodetectors, resulting in a blue shift in the cutoff wavelength from 1100 nm in pristine TiS_3 nanoribbons to 450 nm following oxidation.[58] In particular, thermal treatments oxidized exposed TiS_3 nanoribbons, whereas hBN-encapsulated TiS_3 nanoribbons showed no change following the same treatment, thus enabling selective oxidation and patterning.[58] In another example, Jin *et al.* partially oxidized HfS_2 to form HfO_x, resulting in an atomically pristine $WSe_2/HfO_x/HfS_2$ heterostructure that is suitable for use as an artificial synapse.[59] In this case, the HfO_x served as a tunneling dielectric, while the unoxidized HfS_2 acted as a floating gate that enabled read/write operations by modulating the conductivity of the WSe_2 channel.[59] This flash memory device showed excellent multilevel storage behavior, stability over 250 cycles of on/off pulses (V_g = −60 V and +60 V for 2 s, respectively), and a retention time over 2000 s.[59] Finally, Liu *et al.* adopted a similar scheme, taking advantage of morphotaxial oxidation of 2D $HfSe_2$ to form a $Ti/HfSe_xO_y/HfSe_2/Au$ device *via* oxygen plasma treatment to increase the cell resistance.[60] Memristors fabricated in this fashion exhibited low voltages for resistive switching (<3 V), large switching windows ($>10^3$), and retention times over 15 000 s. These devices also possessed operating currents (100 pA) that were much lower than competing TMDC/TMO memristors (10−100 μA) or other 2D material memristors (0.1−1 μA), resulting in ultralow power consumption (0.1 fJ to 0.1 pJ).[60]

Lateral TMDC−TMO Heterostructures. In addition to vertical heterostructures, lateral TMDC−TMO heterostructures have also been formed through morphotaxial oxidation. For example, Liu *et al.* reported thermal oxidation (thermodynamic regime) of WSe_2 nanosheets exfoliated on Si/SiO_2, as opposed to the shorter and more aggressive oxygen plasma or ozone treatments (kinetic regime) covered in the previous section.[61] In the thermodynamic regime, oxidation initiated from the nanosheet edges and propagated laterally, forming a lateral WSe_2-WO_3 heterojunction with a more conductive substoichiometric WO_{3-x} interfacial region. By tuning the thermal oxidation time, complex lateral heterostructures were formed for WSe_2-WO_{3-x} (semiconducting−conducting) or $WSe_2-WO_{3-x}-WO_3$ (semiconducting−conducting−insulating), as evidenced by Raman spectroscopy and microwave impedance microscopy.[61] This effect was also utilized for CVD-grown monolayer WSe_2, where heating WSe_2-based FETs at 250 °C in air increased the on-current by a factor of 4000, resulting in on/off ratios of up to 5×10^8 and mobilities of 31 $cm^2\ V^{-1}\ s^{-1}$.[62] This improvement was attributed to the formation of WO_{3-x} that p-type dopes the remaining WSe_2 and shortens the FET channel length with highly conductive domains of substoichiometric tungsten oxide. The randomly distributed WO_{3-x} growth observed by Liu *et al.* may be due to the smaller grain sizes and correspondingly higher grain boundary densities for CVD-grown WSe_2, as oxidation proceeds preferentially at grain boundaries. On the other hand, Hoffman *et al.* formed lateral WSe_2-WO_{3-x} heterostructures by selective oxidation of the top 1−2 layers of exfoliated WSe_2 flakes using metallic contacts as an etch mask.[63] In this case, the optimal geometry was formed by exposing the entire channel and the WSe_2 under one electrode to the oxygen plasma treatment, resulting in a p−n junction with an on/off ratio of 333 at −20 V gate bias.[63]

Memristive behavior in WSe_2 has also been engineered *via* oxidation, showing significant promise as a morphotaxial approach for neuromorphic computing. In particular, Lin *et al.* reported that the formation of WSe_yO_x following ozone exposure, and lower-power oxygen plasma treatments resulted in memristive switching behavior with vertical transport as well

https://doi.org/10.1021/acsnano.2c00243
ACS Nano 2022, 16, 7144−7167

as p-type doping of lateral WSe_2 FETs.[64] Similar heterostructures were used by He *et al.* to fabricate synaptic devices, with the ability to modulate memristive behavior with a global back gate on *p*-Si or a top gate upon visible irradiation.[65] The resulting device showed reproducible hysteric behavior for up to 100 voltage sweeps (0 V → 5 V → −5 V → 0 V) and functioned as a multigate memristive synapse that emulates neural synaptic functions such as synaptic plasticity.[65]

Oxidation of Post-TMDC Materials. While TMDC-based oxidation has been the primary focus of oxidation-based morphotaxy, layered materials based on groups 13, 14, and 15 elements are generally more reactive, leading to additional oxidation pathways in these post-TMDC compounds. For instance, Pei *et al.* reported the controlled oxidation of phosphorene (black phosphorus, BP) samples following an oxygen plasma treatment that formed a PO_x protective layer in the process.[66] This encapsulation layer suppressed further ambient oxidation of the underlying BP layers as evidenced by measurable PL over the course of days as opposed to hours for the case of pristine BP. The PO_x layer also served as a buffer layer for subsequent atomic layer deposition (ALD) growth of Al_2O_3 for further passivation. The authors also used this technique to selectively introduce oxygen defects in a phosphorene-based metal-oxide-semiconductor structure that exhibited defect-based PL that could be tuned with back gating.[66] Dickerson *et al.* built upon this approach to fabricate BP FETs with PO_x layers that possess excellent dielectric properties ($\kappa \approx 19$).[67] This device geometry took advantage of the low defect density at the BP−PO_x interface to achieve room-temperature top-gate mobilities of 115 $cm^2\ V^{-1}\ s^{-1}$ with on/off ratios exceeding 300.[67]

Morphotaxial oxidation can also passivate InSe transistors and tune the properties of InSe-based devices. Specifically, a dry surface oxide treatment on InSe was reported by Ho *et al.*, resulting in FETs with mobilities of 423 $cm^2\ V^{-1}\ s^{-1}$ at room temperature and 1006 $cm^2\ V^{-1}\ s^{-1}$ at liquid nitrogen temperatures without the need for further encapsulation (Figure 2C).[68] Moreover, the FETs possessed on/off ratios in excess of 10^8 and current densities of 365 $\mu A/\mu m$, which outperformed devices that were fabricated without the indium oxide capping layer. This exceptional performance was attributed to both the passivating effects of the indium oxide and the unpinning of the Fermi level at the metal contacts, resulting in lower Schottky barriers (~40 meV).[68] Chen *et al.* extended this work to demonstrate that the Fermi-level depinning effect also occurs in the limit of monolayer indium oxide, resulting in electron mobilities of 2160 $cm^2\ V^{-1}\ s^{-1}$ at 2 K and a contact barrier of 65 meV.[69] Unlike Ho *et al.*, these authors employed a UV-ozone process at 80 °C for 10 s that resulted in finer control over the oxide formation. The propensity of indium selenide to form indium oxides can also be used to tune optical properties. As Balakrishnan *et al.* reported, heating (either through thermal treatment or high laser power) led to the formation of quantum-confined In_2O_3−InSe heterostructures with an increase in the effective band gap compared to InSe alone.[70] This oxidation can also be localized *via* hBN encapsulation or a focused laser beam, resulting in micrometer-scale spatial resolution.

The benefits of self-limiting oxides have also been observed for $SnSe_2$, as Paolucci *et al.* reported that the formation of a SnO_2 layer on top of $SnSe_{2-x}$ resulted in an effective gas sensing heterostructure.[71] Compared to stoichiometric $SnSe_2$ devices that exhibited no gas detection, the $SnO_2/SnSe_{2-x}$ heterostructures showed sensitivities of 1.06/ppm and 0.43/ppm for NO_2 and H_2, respectively, with limits of detection of 0.36 and 3.6 ppm, respectively. These heterostructures showed stable operation in ambient conditions for more than six months, which the authors attributed to the air-stable SnO_2 encapsulation layer.[71]

Fundamental Studies of Morphotaxial Oxidation. Since the techniques used to oxidize 2D materials can lead to drastically different results depending on the starting material and oxidation conditions, fundamental work investigating morphotaxial oxidation can provide important guidance for future efforts. For example, Yoon *et al.* investigated the formation of oxides on MoS_2 with electron microscopy, revealing that thermal oxidation is initiated at 400 °C and forms orthorhombic α-MoO_3 with six different orientations on top of the underlying MoS_2.[72] Furthermore, the authors showed that the shape of the MoO_3 domains depends on the supporting substrate for MoS_2, with freestanding MoS_2 forming faceted MoO_3 nanosheets while MoS_2 on silicon nitride resulted in dendritic MoO_3 nanosheets. This dendritic morphology was attributed to a deficiency in oxygen supply resulting in a kinetic, instead of a thermodynamic, oxidation of MoS_2.[72]

First-principles calculations also play an essential role in explaining and predicting experimental results. In particular, Das *et al.* considered the growth of oxides on WSe_2 with *ab initio* calculations, noting that trigonal prismatic TMDCs lead to preferential triangular growth of oxide islands.[73] These authors further showed that oxygen preferentially substitutes at selenium zigzag edges and is energetically more stable in a triangular, rather than a rectangular island. The triangular oxide islands have been predicted to function as embedded quantum dots in WSe_2, suggesting further innovations in TMDC−TMO heterostructures.[73] In related work, Xu *et al.* utilized WO_x as contacts in bilayer WSe_2 FETs, where they argued that the substoichiometric, high work function $WO_{2.57}$ offered decreased contact resistance and enhanced channel current, with conductivities as high as 2600 S m^{-1}.[74] In line with these experimental results, DFT calculations showed that the substoichiometric oxide formed through air exposure gives rise to a defect band near the Fermi energy, resulting in gap-state-assisted carrier transport and enhanced conductivities.[74]

Understanding the oxidation mechanisms can also play a critical role in guiding subsequent experimental work. Along these lines, Longo *et al.* studied the air stability of TMDCs with density functional theory (DFT) and X-ray photoelectron spectroscopy (XPS).[75] They found that basal plane oxidation occurs slowly for both sulfides and selenides, albeit for different reasons. For the case of sulfides, the adsorption energy of an oxygen adatom is negative, making it favorable, although there is a kinetic barrier for subsequent O_2 dissociation and chemisorption. On the other hand, for the case of selenides, the oxygen adatom adsorption energy is positive, making it unfavorable, but the kinetic barrier for subsequent O_2 dissociation is lower than that of the sulfides. They further noted that any surface defects will increase the rate of oxygen dissociation, resulting in higher oxidation rates, and that the oxygen adsorption energies are far more negative for edge states than basal states.[75] In related experimental work, Gronborg *et al.* reported that an excess of edge sulfur species during MoS_2 synthesis resulted in passivation of the edges and limited oxidation to the basal plane, with sulfur in the upper plane exchanging with oxygen.[76] Scanning tunneling micros-

https://doi.org/10.1021/acsnano.2c00243
ACS Nano 2022, 16, 7144−7167

copy (STM) showed that on the Mo edge, Mo is capped by S_2 dimers that are formed by the excess sulfur, which are far less reactive to oxygen than in the uncapped case. Furthermore, STM revealed that oxygen substitutions occurred following both oxygen and water exposure, with an activation barrier of ~0.79 eV in the case of oxygen.[76] These insights will help inform effective synthetic conditions and subsequent treatments to obtain desired morphotaxial structures.

Understanding the mechanism of the edge oxidation in TMDCs is another area of recent interest. Using STM, Park *et al.* observed that air exposure of WSe_2 grown on highly oriented pyrolytic graphite resulted in an expanded band gap at edge sites.[77] Normalized differential tunneling conductance spectra showed that the band gap of the monolayer edge states transitioned from being narrower than the monolayer terrace states (1.06 eV versus 2.18 eV, respectively) to much wider (3.15 eV versus 2.07 eV) following oxidation. The observed edge band gap was close to the theoretical band gap of WO_3, suggesting complete conversion of the edge to an oxide.[77] Addou *et al.* studied a similar system but found that the step edges of WSe_2 following exposure to ambient air formed $WO_{2.7}$ with metallic edge states.[78] Contrary to Park *et al.*, the authors focused on the smaller features in the middle of the band gap and observed metallic behavior for the flake edges with a V-shaped density of states. The resulting metallic edge can be regarded as a 1D conducting wire in close contact with the 2D semiconducting WSe_2, thus forming a lateral metal−semiconductor heterojunction. Subsequent DFT calculations showed that oxidation occurs preferentially along W-terminated edges and that substoichiometric, metallic WO_x ($x < 3$) is preferred over semiconducting, stoichiometric WO_3, confirming the experimental observations of metallic edges.[78]

Fundamental studies of oxidation have also been performed for post-TMDC 2D materials. For instance, black phosphorus has been theoretically shown by Ziletti *et al.* to form planar and tubular oxides and suboxides that have varying band gaps depending on the oxygen concentration.[79] Using DFT, the authors showed that fully saturated P_2O_5 offers an insulating native oxide that is transparent in the near UV with a bandgap of 8.5 eV in addition to acting as an effective encapsulation layer.[79] Kuntz *et al.* built upon this theoretical understanding of phosphorene-based oxidation by experimentally investigating the difference between water-based and oxygen-based oxidation pathways on liquid-phase exfoliated BP.[80] They discovered that oxidation with O_2 proceeds along the basal surface, whereas H_2O preferentially oxidizes defect sites (such as on the edges), thus providing an avenue for basal or edge selective oxidation of BP.[80]

Patterning Schemes. The relative ease of controlling oxidation in layered materials enables patterning *via* various writing and masking techniques. These spatially defined morphotaxial techniques provide opportunities for forming abrupt discontinuities in flake thickness in addition to FET stacks that would otherwise be challenging to fabricate.

Since many vdW materials possess thickness-dependent electronic properties, it is appealing to form homojunctions out of the same material but with differing thicknesses. Toward this end, Robbins *et al.* reported high spatial resolution thinning (sub-150 nm lateral features) of black phosphorus *via* EBL patterning combined with use of Al_2O_3 masking.[81] This procedure resulted in FETs that showed increased on/off ratios compared to uniformly thick BP devices (Figure 2D).[81] Patterning and thinning can also occur without the aid of a mask, as Liu *et al.* demonstrated a scanning probe nanolithography method using conductive atomic force microscopy to oxidize sections of BP that can be readily removed with water rinsing.[82] This technique was tuned by applying precise voltage biases to modulate the oxide depth with nanoscale lateral resolution provided by the AFM tip. Furthermore, by using AC biases, BP was directly patterned on SiO_2 substrates, which enabled FETs with a 50-fold increase in on/off ratio compared to unpatterned BP (Figure 2E).[82] Direct patterning has also been achieved with laser oxidation, as Lu *et al.* showed that laser thinning of BP allows tunable thicknesses with a spatial resolution of ~0.5 μm.[83] In this case, the authors also found an increase in FET on/off ratio from ~10 to ~10^3, which they attributed to the larger band gap in thinned few-layer BP.[83]

While BP is an attractive target for patterning schemes due to its ease of oxidation in ambient conditions, direct patterning of TMDCs by EBL or scanning probe lithography has also been demonstrated. For example, Dago *et al.* demonstrated direct patterning of p-type WSe_2 through a combination of oxygen plasma treatments and scanning probe lithography.[84] After forming a self-limiting oxide layer that doped the underlying WSe_2 using an initial oxygen plasma treatment, the application of an electrical bias with conductive AFM allowed the growth of patterned local WSe_2 oxides that were subsequently removed through water immersion. This procedure enabled the formation of FETs with 5 parallel 250 nm half-pitch nanoribbons.[84] This strategy has been applied to MoS_2 by Ryu *et al.*, where they fabricated an array of 17 MoS_2 nanoribbons with 300 nm half-pitch in addition to demonstrating that the spatial resolution of oxidative scanning probe lithography can be as precise as 10 nm.[85]

Finally, oxygen plasma treatments also enable the synthesis of WSe_2 lateral homojunctions. In particular, Mitta *et al.* used an EBL-based scheme to pattern regions exposed to oxygen plasma, resulting in a WO_x layer that acted as a p-type dopant for the normally n-type WSe_2.[86] The resulting WSe_2 p−n junction exhibited improved photoresponsivity (2000 mA/W at 852 nm), higher external quantum efficiency (420%), and enhanced detectivity (7.2×10^{10} Jones) compared to native n-type WSe_2. Scanning photocurrent microscopy further confirmed that the photocurrent is generated mostly from the p−n junction of WSe_2 at zero gate bias, demonstrating the utility of spatially defined morphotaxial oxidation for WSe_2 optoelectronic applications.[86]

MORPHOTAXIAL ANIONIC MODIFICATIONS

Since oxidation-based modifications have been widely and successfully studied, it is reasonable to expect that expanding the range of anionic modifications beyond oxygen would create additional opportunities for structure and property modification. Indeed, the field of morphotaxial anionic modifications is rich with promising synthetic approaches. This section covers emerging work on anionic modification schemes, starting with the simplest case of chalcogen-based modifications of TMDCs. This class of morphotaxial anionic modification ranges from chalcogen removal to sulfurization and selenization. By performing morphotaxial anionic modifications on only one side of a TMDC monolayer, it is further possible to form 2D Janus structures that break symmetry in the out-of-plane direction. Finally, by employing anionic-substitution reactions beyond chalcogens, a much broader range of morphotaxially derived 2D materials can be realized.

https://doi.org/10.1021/acsnano.2c00243
ACS Nano 2022, 16, 7144−7167

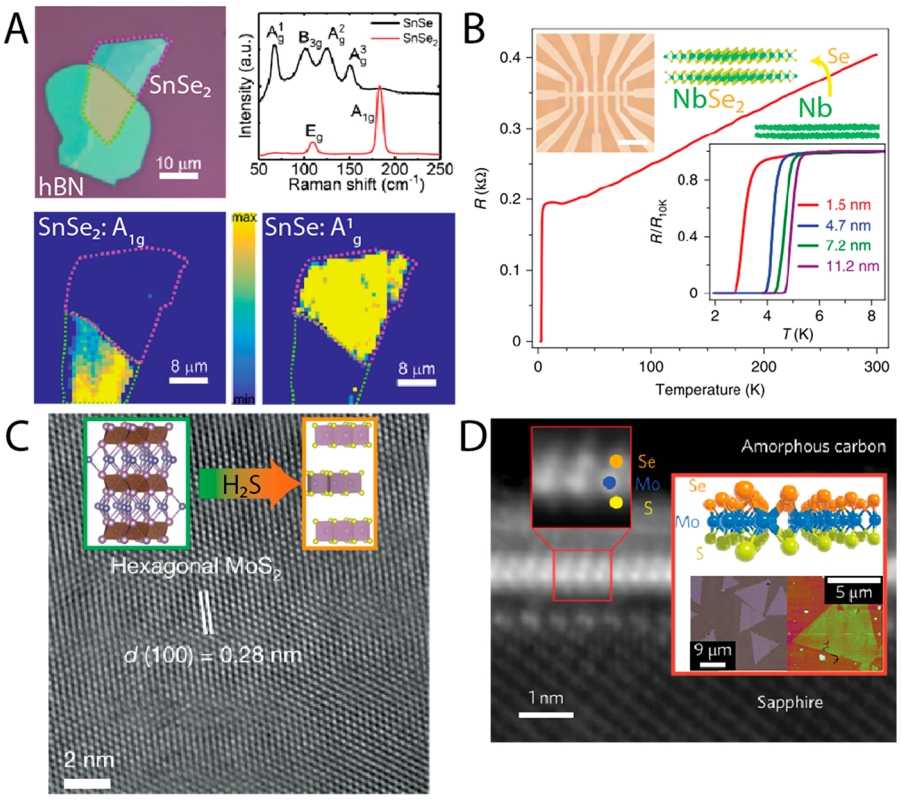

Figure 3. Chalcogen-based morphotaxy. (A) Optical and Raman microscopy of a $SnSe_2$−SnSe p−n heterojunction. The heterojunction is formed by capping the bottom part of the $SnSe_2$ layer with a hBN layer, and then thermally converting the uncapped section. Raman mapping shows the A_{1g} mode from $SnSe_2$ (L) and A^1_g mode from SnSe (R), thus confirming that the capped section remains $SnSe_2$ while the uncapped portion is fully converted to SnSe. Reproduced with permission from ref 90. Copyright 2018 American Chemical Society. (B) Selenization of a sputtered Nb film results in 2D superconducting $NbSe_2$. The superconducting transition temperature (T_c) shows a strong dependence on film thickness. Adapted with permission from ref 101. Copyright 2019 Springer Nature. (C) Conversion of a non-vdW solid (Mo_2GeC) into a layered vdW solid (MoS_2) following H_2S treatment. High-resolution TEM confirms the crystallinity of the final vdW material. Adapted with permission from ref 112. Copyright 2020 Springer Nature. (D) Synthesis of the Janus monolayer MoSSe by plasma stripping the top layer of sulfur from CVD-grown MoS_2 followed by a thermal selenization step. Cross-sectional annular dark-field scanning transmission electron microscopy shows the asymmetric MoSSe structure. Reproduced with permission from ref 87. Copyright 2017 Springer Nature.

Chalcogen-Based Modifications. Due to the vast literature on 2D chalcogenides, many anionic modifications have focused on chalcogen chemistry, such as removing chalcogens from parent 2D chalcogenides or adding chalcogens to TMOs or TMDCs. These chalcogen-based modifications have enabled diverse applications ranging from Li-ion batteries to symmetry breaking polarization in the Janus TMDC MoSSe.[87]

Chalcogen Sublimation. Removal of chalcogens from parent 2D chalcogenides can be achieved by introducing sufficient energy, usually through thermal treatments. For instance, Jiang *et al.* showed that a composite of SnS_2 and reduced graphene oxide (rGO) can be converted into SnS and sulfur-doped graphene at 500 °C in an inert atmosphere.[88] This reaction plays two synergistic roles, namely, removing sulfur improves the gravimetric lithiation capacity of the SnS_2 starting material by reducing the active material mass and doping rGO with sulfur passivates defects that would otherwise be lithium trapping sites while also providing a conductive network. The result is a composite Li-ion battery anode that shows excellent cycling stability of 803.7 mA h g^{-1} after 100 cycles at 0.1 A g^{-1} and rate capability of up to 10*C* (where *C* is defined as 1000 mA g^{-1} in this case).[88] Similarly, Zhou *et al.* reported improvement in anode performance for sodium-ion batteries, where SnS_2 mixed with graphene was annealed in argon at 600 °C to form a SnS−graphene composite.[89] The SnS−graphene composite yielded superior rate capability (940 mA h g^{-1} at 30 mA g^{-1} and 308 mA h g^{-1} at 7290 mA g^{-1}) and cycling performance when compared to SnS_2−graphene or SnS_2 anodes. This improved performance was attributed to orthorhombic SnS being less structurally affected during sodiation compared to hexagonal SnS_2, with the additional benefit of adopting the parent SnS_2 nanosheet morphology.[89]

Chalcogen removal has also proven to be beneficial for electronic and optoelectronic devices. In particular, Tian *et al.* formed a lateral heterostructure of n-type $SnSe_2$ and p-type SnSe by thermal annealing at 300 °C for 200 min, with hBN covering the regions designated as n-type $SnSe_2$ (Figure 3A).[90] This scheme enabled precise masking by inhibiting selenium sublimation only where hBN is present, resulting in atomically sharp lateral p−n heterostructures as evidenced by Raman spectroscopy.[90] Thermal annealing in vacuum has also been used to control stoichiometry as Voznyi *et al.* took advantage of the relative ease of sulfur sublimation to obtain monophasic SnS films from a starting layer of SnS_2.[91] The resulting SnS layer exhibited no secondary phase as would be expected if it were grown using more traditional methods such as thermal evaporation or atomic layer deposition. In addition, the SnS

https://doi.org/10.1021/acsnano.2c00243
ACS Nano 2022, 16, 7144−7167

film adopted the morphology of the original SnS_2 layer, which was then employed in glass/ITO/CdS/SnS/Sn solar cells.[91] This approach illustrates the benefits of achieving well-defined ultrathin films using morphotaxial chalcogen sublimation.

Chalcogen removal can also achieve 2D phases of non-vdW materials. Specifically, Ryu *et al.* reported the morphotaxial phase transformation of layered vdW $PtSe_2$ into 2D PtSe, which is not a layered vdW material in the bulk.[92] In this case, the authors used *in situ* thermal annealing to observe the phase transition with aberration-corrected annular dark field scanning transmission electron microscopy (STEM), which revealed that few-layered $PtSe_2$ undergoes Se loss at 550 °C that results in ultrathin PtSe crystals. By controlling the temperature, they found that both the Pt and Se atoms migrate and are completely reconstituted to form the PtSe phase in bilayers that are stacked in an AA pattern.[92]

In addition to thermal treatments, chalcogen sublimation can also be promoted by electron-beam irradiation. For example, Sutter *et al.* used high-resolution TEM to observe electron-beam removal of chalcogen atoms in SnS_2 and $SnSe_2$, resulting in the formation of their monochalcogenide counterparts.[93] For the case of $SnSe_2$, electron irradiation uniformly resulted in basal plane oriented SnSe, similar to other examples of chalcogen-removal morphotaxy. However, for the case of SnS_2, while thin layers of SnS_2 transformed into basal plane oriented SnS, thicker layers of SnS_2 instead transformed into SnS that was oriented along the [011] direction. This observation was explained by the formation of an intermediate, metastable Sn_2S_3 phase that only occurs for SnS_2 thicknesses above 3 layers.[93] This work shows that in addition to stoichiometry, morphotaxial transformations can also be controlled by geometrical parameters such as the thickness and orientation of the starting layered material.

Sulfurization and Selenization. The opposite approach of adding chalcogens through sulfurization or selenization can also serve as a morphotaxial pathway for synthesizing ultrathin films. Common examples include adding chalcogens to films of transition metal oxides and transition metals. In addition, sulfurization and selenization can be used to selectively transform portions of layered materials into stoichiometrically different compounds or for converting non-vdW structures into layered vdW materials.

One widely employed application of sulfurization is the conversion of MoO_3 to obtain wafer-scale MoS_2. In particular, Lin *et al.* converted thermally deposited MoO_3 on *c*-face sapphire into uniformly thick three-layer MoS_2 films using a reduction step (500 °C in 20% H_2/Ar) followed by sulfurization (1000 °C with sulfur).[94] FETs fabricated from these MoS_2 films showed on/off ratios of 10^5 and mobilities of 0.8 $cm^2\ V^{-1}\ s^{-1}$.[94] In related work, Taheri *et al.* explored the growth mechanism of MoO_3 sulfurization, leading to the conclusion that ultrathin MoO_3 films (0.5−1 nm) grown by electron-beam evaporation in a two-zone heating system allows the synthesis of nearly void-free, monolayer MoS_2.[95] In this case, the MoO_3 served as a source of Mo upon vaporization, which easily diffused across the substrate and reacted with sulfur to form local islands of MoS_2 that then merged to form a continuous monolayer.[95] Conversely, Wang *et al.* reported a more traditional form of morphotaxy by converting MoO_2 microcrystals into MoS_2 flakes *via* layer-by-layer sulfurization.[96] The resulting MoS_2 nanosheets adopted the rhombohedral shape of the MoO_2 microcrystals and could be peeled off from the parent MoO_2 crystal using a polymer film. This layer-by-layer sulfurization allowed for precise control of the MoS_2 layer number and resulted in micrometer-scale MoS_2 nanosheets with high crystallinity. FETs fabricated from these MoS_2 flakes showed high on/off ratios of 10^4−10^6 and mobilities of 0.1−0.7 $cm^2\ V^{-1}\ s^{-1}$.[96] Using a phase-transition-induced growth technique, Sohn *et al.* offered another morphotaxial strategy for controlling the number of MoS_2 layers.[97] By first sputter depositing an energetically unstable amorphous molyoxysulfide (a-MoS_xO_y), the authors synthesized crystalline MoS_2 through a thermal annealing process in a H_2S environment. By controlling the deposition rate, the authors were able to synthesize wafer-scale monolayer MoS_2 by relying on the unbalanced Mo^{5+} states in the original a-MoS_xO_y film to facilitate more uniform growth compared to the sulfurization of Mo^{6+} states in MoO_3.[97]

Morphotaxial chalcogenization can also be employed for the growth of tungsten-based TMDCs from WO_3. For instance, Browning *et al.* showed that hexagonally stabilized tungsten oxide films can undergo Se−O exchange with minimal structural changes, resulting in highly uniform WSe_2 films.[98] By treating the as-deposited amorphous WO_3 with a rapid thermal anneal at 600 °C, the researchers obtained a metastable crystalline phase that can be morphotaxially converted to WSe_2 as thin as 3 layers.[98] Tin oxides can also be converted to sulfides for use as sodium-ion battery anodes. By annealing SnO_2−carbon composites with sulfur powder, Yang *et al.* achieved SnS_2−carbon particles that retained the original core−shell structure of the starting SnO_2−carbon particles.[99] This sulfurization scheme allowed for complete conversion into SnS_2, which was found to have a higher reversible capacity of 770 mA h g^{-1} compared to 360 mA h g^{-1} for the parent oxide.[99]

In addition to morphotaxial conversion of oxides, some chalcogenides can be prepared by morphotaxial conversion of metals. Using a plasma-assisted process, Su *et al.* selenized a film of Pt to form large-area $PtSe_2$ films at 100 °C.[100] The researchers converted the initial Pt film into few-layer, semiconducting $PtSe_2$, although with limited gate tunability (on/off ratios only up to 16). Nevertheless, a $PtSe_2$ photodetector was fabricated on a flexible polyimide substrate using this method that had a wide optical absorption range due to the low bandgap of $PtSe_2$ as well as excellent photoresponsivity stability (0.1 to 0.4 A W^{-1}) following 1000 bending cycles (radius ∼0.4 cm) with a photocurrent of up to 9 μA when illuminated at 408 nm.[100] High-quality, superconducting films of $NbSe_2$ have also been grown using a selenization-based approach, as demonstrated by Lin *et al.*[101] In this case, a sputtered Nb film was reacted with selenium, resulting in a structural transformation into $NbSe_2$, as evidenced by the increase in thickness from 0.7 to 1.5 nm, while retaining large-scale homogeneity with low roughness. Furthermore, $NbSe_2$ films prepared in this way were more environmentally stable compared to their CVD-grown counterparts, with no change in Raman signals or thickness after heating in air. The $NbSe_2$ films also possessed superconducting behavior at cryogenic temperatures with the superconducting critical temperature (T_c) increasing with increasing film thickness (Figure 3B). In particular, bilayer $NbSe_2$ had a T_c of 2.8 K, which only decreased slightly upon exposure to air despite being heated and further showed stability in a variety of different solution baths (*e.g.*, NaOH, HF, and HCl) or when annealed in vacuum at temperatures up to 430 °C. The authors also reported a similar scheme for realizing environmentally

https://doi.org/10.1021/acsnano.2c00243
ACS Nano 2022, 16, 7144−7167

stable $TiSe_2$ and other ambient-sensitive selenides. Starting with another transition metal, Yang *et al.* reported the synthesis of semiconducting Cu_2Se *via* selenization of Cu(111) in ultrahigh vacuum, resulting in a layered phase of Cu_2Se that was markedly distinct from its regular unlayered bulk phase.[102] This 2D Cu_2Se structure exhibited a band gap of 0.74 eV, again underscoring that phases distinct from naturally occurring materials can emerge using morphotaxial approaches. Finally, recent work by Zheng *et al.* demonstrated the tellurization of thin Pd films by reacting with Te vapor at 300 °C.[103] The resulting $PdTe_2$ showed higher conductivity (4.3×10^6 S m^{-1}) compared to the starting Pd film (3.0×10^6 S m^{-1}) and also resulted in reduced contact resistances for $MoTe_2$ and WSe_2 FETs.[103]

Morphotaxial chalcogenization is not only limited to complete conversions but can also allow for more subtle phase control. For example, Ghosh *et al.* reported that large-area, CVD-grown $MoSe_2$ can be thermally converted into MoS_2 in the presence of sulfur at 850 °C, with photoluminescence measurements revealing that the conversion occurs with no intermediate MoS_xSe_y species, as evidenced by the emergence of a MoS_2 PL peak without a gradual shifting from the $MoSe_2$ peak.[104] This relatively abrupt conversion was also observed by Su *et al.*, who found that in both cases of MoS_2 and $MoSe_2$, the corresponding conversion occurs completely at high temperatures (800−900 °C).[105] However, while MoS_2 selenizes into a solid solution of MoS_xSe_y, $MoSe_2$ sulfurizes into largely ordered domains of MoS_2 and $MoSe_2$. These examples indicate the importance of not only processing conditions but also the choice of the starting parent compound in determining the outcome of morphotaxial chalcogenization.[105] Sadler and Kempa explored yet another way of accomplishing biphasic TMDCs by using multiple chalcogen sources in the high-vacuum conversion of bulk Mo oxides.[106] Under a stepwise exposure to selenium and then sulfur at 40 Torr and 400 °C, Mo oxides converted into a biphasic mixture of $MoSe_2$ and MoS_2, as evidenced by Raman spectroscopy. However, under concurrent exposure to both selenium and sulfur, Mo oxide converted to a more complicated structure, with a noticeable broadening of the A_{1g} peak and a shift from 242 to 264 cm^{-1}, indicative of an alloyed structure.[106]

Fundamental understanding of the processes involved in morphotaxial chalcogenization can also help guide the formation of heterostructures and patterned structures by promoting morphotaxy in desired locations. In particular, Afaneh *et al.* utilized a 532 nm laser to locally pattern monolayers of WSe_2 and $MoSe_2$ into their respective sulfides in the presence of H_2S.[107] In this case, the laser plays two roles; namely, local laser heating promotes the formation of selenium vacancies in the transition metal selenides in addition to assisting in the disassociation of H_2S molecules such that free sulfur can then substitute into the vacancies. Further characterization of a laser-patterned WSe_2 monolayer *via* STEM showed nearly complete replacement of selenium with sulfur near the center of the laser spot, indicating that precise control of laser intensity is vital for full conversion.[107] Traditional lithographic techniques can also result in lateral conversion as Kemelbay *et al.* showed the growth of embedded TMDCs through reduction and chalcogenization of TMOs in lithographically defined openings.[108] By varying the oxide thickness, the authors controlled the number of TMDC layers, with the procedure being applicable to MoS_2, $MoSe_2$, WS_2, and WSe_2.[108] A similar approach was utilized by Mahjouri-Samani *et al.* to form $MoSe_2$−MoS_2 or WSe_2−WS_2 heterojunctions *via* pulsed laser vaporization.[109] In this case, the researchers used EBL to pattern monolayer flakes followed by the deposition of a protective SiO_2 layer. With appropriate care to expose the $MoSe_2$ flake to sufficiently high temperatures and sulfur concentrations (700 °C with 400 sulfur pulses), complete conversion occurred in the unmasked regions with no intermediate phases of MoS_xSe_{2-x} being formed. The authors showed that the resulting MoS_2−$MoSe_2$ heterojunction possessed a sharp (∼5 nm) heterointerface with a type-I band alignment.[109] Li *et al.* explored an alternative pathway to lateral heterojunctions by using the relative difference in reactivity of MoS_2 monolayers and bilayers to selectively substitute Se atoms on the monolayer while the bilayer region remained pure MoS_2.[110] With maintenance of the Se substitution temperature in the range between 740 and 810 °C, the monolayer was continuously tuned from MoS_2 to $MoS_{2-x}Se_x$, as evidenced by Raman and PL spectroscopy.[110]

Finally, morphotaxial chalcogenization is not restricted to TMDCs and TMOs. In particular, Li *et al.* synthesized a 2D vdW lateral heterojunction of SnS grown by molecular beam epitaxy and a monolayer of SnS_2 formed by sulfurization.[111] Interestingly, this process was found to be thermally reversible as annealing of SnS_2 resulted in the formation of the parent SnS compound. In addition, the heterostructure between SnS and SnS_2 possessed a twist angle of ∼15° as revealed by STM while scanning tunneling spectroscopy showed a type II band alignment.[111] In another example, Du *et al.* investigated MAX structures (M = early transition metal, A = group 13−16 element, X = B, C, N, Si) as a scaffold to obtain TMDCs *via* reactions with chalcogen-containing vapors (H_yZ, where Z = S, Se, or Te) such as the conversion of Mo_2GeC to MoS_2 following reaction with H_2S (Figure 3C).[112] This approach showed that a non-vdW solid can be converted completely into a vdW solid, resulting in high-quality layered structures. Using these principles, the authors synthesized 13 distinct TMDCs of various compositions and phases, illustrating the broad generality of this approach.[112]

Janus Structures. One additional application of the removal of chalcogens and subsequent chalcogenization of TMDCs is the formation of Janus structures. Janus 2D van der Waals materials feature asymmetric facial properties achieved by functionalization or exchange of atoms of only one side of the material, in most cases the side facing up from the substrate.[113] Unlike other alloys accomplished *via* spatially random chalcogenization, Janus structures consist of complete functionalization or exchange of one anion on one side of the nanosheet without affecting the other side, resulting in exotic physics from the broken out-of-plane symmetry, such as large polarization fields, ferromagnetic ordering at high temperatures, skyrmion formation, and excitonic behavior, that differs from symmetric structures.[114] However, the difficulty in synthesizing Janus structures has led to these types of materials being relatively understudied, with morphotaxial principles proving crucial in experimentally realizing these materials. In contrast to other 2D materials that can be synthesized using top-down or bottom-up approaches, Janus materials have only been synthesized using morphotaxy.

Two groups synthesized a 2D Janus structure in 2017. Zhang *et al.* reported the growth of a sandwiched S−Mo−Se monolayer, where the top layer of selenium atoms in monolayer $MoSe_2$ was controllably sulfurized by heating at

https://doi.org/10.1021/acsnano.2c00243
ACS Nano 2022, 16, 7144−7167

800 °C.[115] Subsequent Raman and secondary ion mass spectrometry (SIMS) analyses demonstrated the existence of S−Mo−Se atomic stacking as opposed to a randomly alloyed MoS_xSe_{2-x} or biphasic $MoSe_2$−MoS_2 material. Computational studies performed by the same group suggested lower basal plane hydrogen evolution reaction (HER) overpotentials when compared to traditional TMDCs, indicating possible applications for the 2D Janus material.[115] Lu *et al.* also reported a similar synthesis scheme, where they started with a MoS_2 monolayer and promoted selenization of the top layer with a remote hydrogen plasma treatment (Figure 3D).[87] This synthetic pathway was achieved at a lower temperature of 350 °C due to the formation of an intermediate H−Mo−S phase after the plasma treatment. The final MoSSe Janus structure was shown to have clear out-of-plane asymmetry, as probed with angle-resolved second harmonic generation and resonance-enhanced piezoresponse force microscopy.[87]

While the initial 2017 reports of Janus structures based on MoSSe were promising, a few years passed before more experimental reports were published, presumably due to the challenging synthesis of Janus structures. Recent reports have explored strategies to make Janus synthesis more reliable and to realize additional 2D Janus structures. For example, Lin *et al.* utilized a low energy selenium replacement scheme in WS_2 to synthesize a Janus WSSe structure.[116] Using pulsed laser deposition (PLD) to form a selenium plasma that was exposed to a monolayer of WS_2, the authors achieved the Janus WSSe structure at a relatively low temperature of ∼300 °C.[116] This work was augmented with molecular dynamics simulations of Se_2 and Se_9 clusters to identify the kinetic energies required to displace a sulfur atom without sputtering away the underlying tungsten.[116] Trivedi *et al.* also accomplished a room-temperature synthesis of Janus TMDCs including the Janus WSSe structure.[114] Using a selective epitaxy atomic replacement process, the authors formed selenium vacancies on selenium-based TMDCs through exposure to hydrogen radicals and then reacted the selenium-depleted monolayer with low-energy reactive sulfur radicals. Due to the mild processing conditions, Trivedi *et al.* took this synthesis one step further to form lateral and vertical heterostructures of 2D Janus layers with WSSe and MoSSe, which would otherwise alloy at higher temperatures. Subsequent PL characterization revealed that the two regions exhibited distinct peaks, indicating that the Janus TMDC heterostructures were biphasic.[114] Further work on coupling Janus MoSSe with traditional TMDC materials has been enabled by these low-temperature synthesis methods, such as Zhang *et al.* reporting the enhancement of the vdW interlayer coupling between MoSSe and MoS_2.[117] Specifically, the out-of-plane dipole moment in MoSSe leads to a built-in electric field that enhanced the vdW coupling in MoSSe−MoS_2 heterostructures by 13.2%, offering additional parameters to tune heterostructure coupling and valley degrees of freedom in symmetric TMDCs. This work was enabled by a similar scheme to that of Trivedi *et al.*, where Zhang *et al.* stripped away the top layer of sulfur in bilayer MoS_2 and subsequently performed a selenization treatment. This procedure formed a MoSSe−MoS_2 heterostructure without the need for subsequent transfer and assembly.[117]

Finally, it is important to note that experimental work on Janus structures is not confined to MoSSe and WSSe, with more recent research being focused on different cation/anion combinations. For instance, Sant *et al.* reported the synthesis of PtSSe by sulfurizing $PtSe_2$ grown on Pt(111), employing morphotaxial techniques in both the synthesis of the $PtSe_2$ (selenization of Pt) and conversion to PtSSe (sulfurization of $PtSe_2$ by heating in H_2S).[118] To confirm the formation of the Janus structure, the authors performed angle-resolved XPS, demonstrating the preferential substitution of S in the top layer of $PtSe_2$.[118] The experimental investigation of 2D Janus materials is still ongoing, and reports on fundamental properties of Janus layers such as the study of Petrić *et al.* of the Raman response of MoSSe and WSSe monolayers[119] will likely accelerate progress in this field. Due to the lack of naturally occurring 2D Janus materials, refined morphotaxial synthetic procedures will also be enabling. Hajra *et al.* expanded the definition of Janus vdW materials by reporting the synthesis of Janus BiTeCl and BiTeBr sheets by morphotaxially converting Bi_2Te_3 *via* exposure to BiX_3 or BiX_3 (X = Cl, Br) vapor.[120] Unlike Janus TMDCs that are not found in nature, BiTeCl and BiTeBr have been studied experimentally on mechanically exfoliated bulk crystals with spin-polarized Rashba states being observed due to the large spin−orbit coupling originating from the heavy bismuth atoms. The work of Hajra *et al.* enabled the synthesis of large-area thin films of BiTeCl and BiTeBr, taking advantage of the similar, but not identical, crystal symmetry between Bi_2Te_3 and BiTeX, as evidenced by similar experiments with Sb_2Te_3 not resulting in a SbTeX structure. The authors further reported the conversion of multiple layers of Bi_2Te_3 into BiTeX (here X = Cl or Br), which they attribute to the built-in electric field in a fully converted layer opening up a vdW gap that allows for the intercalation of the X^- ions and conversion of subsequent layers.[120]

Synthesis of Additional 2D Compounds by Morphotaxial Templating. While the vast majority of anionic morphotaxy has focused on modifications to chalcogenides, emerging efforts on carburization, nitridation, and fluorination offer approaches to post-TMDC morphotaxy. Often in these schemes, a layered TMDC or TMO serves as the scaffold to synthesize nonlayered structures that nevertheless retain the original shape of the parent crystal. This approach is especially useful for obtaining MXenes (M = transition metal, X = carbon or nitrogen), which are traditionally obtained by etching a corresponding MAX (A = group IIIA or IV element) structure that results in additional surface termination groups. In this manner, morphotaxy offers the possibility to synthesize 2D analogues of non-vdW structures through morphotaxial templating in an atomically precise fashion.

In the context of carburization, Zhao *et al.* reported the formation of a hybrid nanostructure of MoS_2−Mo_2C on carbon paper by heating at 750 °C in the presence of methane (25 sccm CH_4 with a carrier gas of 400 sccm Ar and 140 sccm H_2).[121] These vertically aligned MoS_2−Mo_2C composites retain the structure of the original MoS_2 nanosheets but with Mo_2C domains appearing in localized regions for methane exposure times less than 60 min followed by MoS_2 nanosheets being completely converted after 60 min. These composites demonstrated lower overpotentials (63 mV) than that of MoS_2 (130 mV) or Mo_2C (146 mV) alone in addition to lower Tafel slopes (53 mV dec^{-1} versus 61 mV dec^{-1} and 63 mV dec^{-1}, respectively), confirming excellent HER performance of this hybrid catalyst.[121] Similarly, Jeon *et al.* synthesized Mo_2C from a MoS_2 parent crystal by thermally annealing under CH_4 and H_2 while using copper foil as a catalyst.[122] Unlike Zhao *et al.*, these authors found that carburization proceeded from the edge of the MoS_2 nanosheets, which they hypothesized occurs

https://doi.org/10.1021/acsnano.2c00243
ACS Nano 2022, 16, 7144−7167

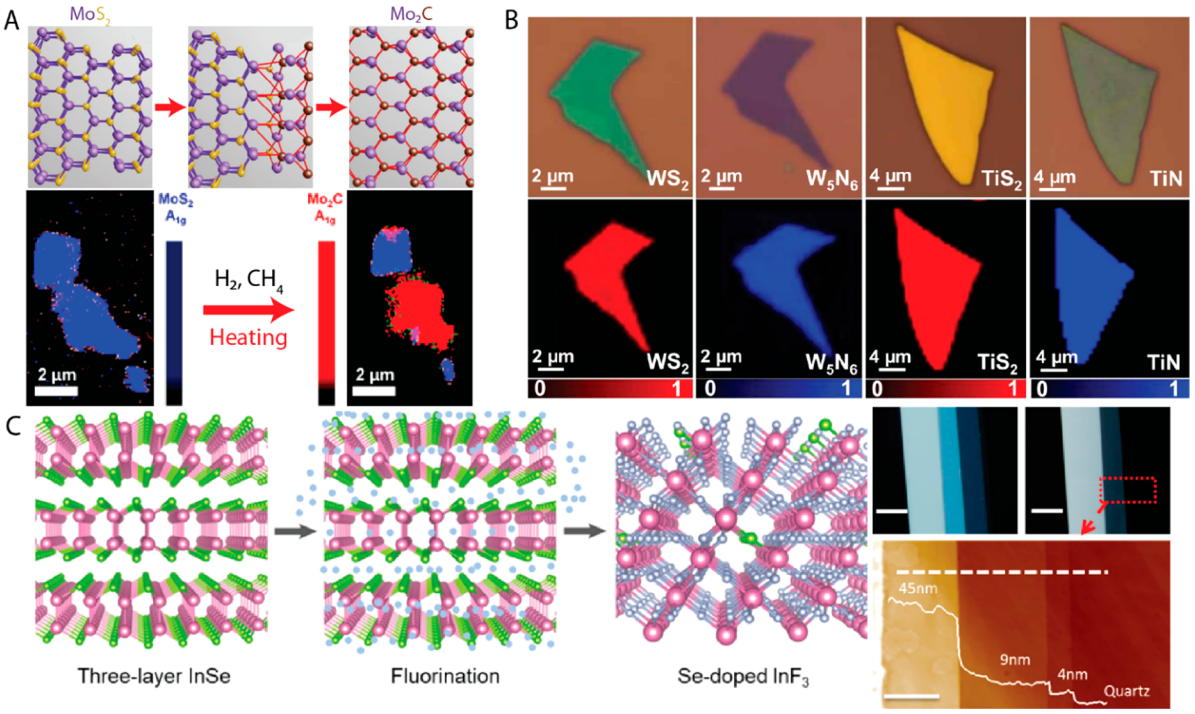

Figure 4. Post-TMDC morphotaxy and templating. (A) Synthesis of Mo_2C *via* thermal annealing of MoS_2 in the presence of methane gas. Raman mapping shows the evolution of MoS_2 into Mo_2C after 3 h of annealing at 820 °C under a CH_4/H_2 flow. Mo_2C formation initiates along the edges of the parent MoS_2 nanosheets. Adapted with permission from ref 122. Copyright 2018 American Chemical Society. (B) Ammonolysis of various TMDCs. The top row contains optical images of WS_2 and TiS_2 before and after the ammonia treatment, while the bottom row shows Raman mapping of the nanosheets. Both rows show complete conversion of the parent TMDC material into a transition metal nitride. Reproduced with permission from ref 124. Distributed by AAAS for use in commercial journals under a Creative Commons Attribution NonCommerical License 3.0 (CC BY-NC). (C) Fluorination of InSe to form non-vdW InF_3. Fluorination of three-layer InSe has been accomplished, resulting in ultrathin InF_3 as demonstrated with optical microscopy and atomic force microscopy. Reproduced with permission from ref 127. Copyright 2019 American Chemical Society.

by the hydrodesulfurization of MoS_2 *via* $H^•$ radicals and subsequent carbide conversion *via* $CH_3^•$ radicals interacting with the Mo-terminated edge (Figure 4A). Subsequent Raman and electron microscopy confirmed the atomically pristine interface between MoS_2 and Mo_2C, with Mo_2C formation proceeding from the edges as predicted. Electrical characterization showed that the Schottky barrier height (26 meV for the lateral Mo_2C-MoS_2 heterojunction) and contact resistance (1.2 kΩ μm) are improved compared to $Ti-MoS_2$ heterojunctions (66 meV and ∼100 kΩ μm, respectively). This work demonstrated a morphotaxial approach to synthesizing atomically sharp semiconducting−metallic heterojunctions that are potentially useful for nanoscale electronic and energy devices.

Layered vdW materials can also be nitrated, often through the reaction of a parent crystal with ammonia. Specifically, Xiao *et al.* reduced 2D hexagonal MoO_3 grown on NaCl by annealing in an NH_3 atmosphere at 650 °C, where subsequent washing of the product in water resulted in 2D MoN aqueous dispersions.[123] Due to the salt-templating of the initial MoO_3 parent crystal, the synthesized MoN is laterally large (on the order of 20 μm), and the authors reported that the salt may act as a further stabilizer to retain the atomically thin structure during ammonization. MoN synthesized in this fashion was used to form flexible solid-state supercapacitors with energy densities of ∼2 mWh cm^{-3} and power densities of 1.5 W cm^{-3}, which are comparable to state-of-the-art Li thin-film batteries for energy density and commercially available supercapacitors for power density.[123] Cao *et al.* further demonstrated that ammonization can be generalized to a wide variety of TMDCs, resulting in diverse 2D transition metal nitrides, such as Mo_5N_6, W_5N_6, and TiN (Figure 4B).[124] In this case, mechanically exfoliated TMDCs were heated at 750 to 800 °C in the presence of ammonia gas, resulting in near complete conversion. Mechanistic studies revealed that despite the layered structure of MoS_2 and nonlayered structure of Mo_5N_6, the layers of Mo atoms are hexagonally patterned, resulting in a structural transformation that retains the original morphology as sulfur is liberated and replaced with nitrogen. Electrical measurements on as-synthesized Mo_5N_6 showed excellent metallic behavior with sheet resistances as low as 100 Ω/square. In addition, subsequent tuning of the conversion parameters resulted in lateral heterostructures between MoS_2 and Mo_5N_6.[124] Ammonization has also been used to morphotaxially transform III−VI compounds such as GaS and GaSe into GaN nanosheets, as reported by Sreedhara *et al.*[125] In particular, micromechanically exfoliated GaS and GaSe were exposed to ammonia at 650 and 600 °C, respectively, to form few-layer GaN nanosheets that showed no trace of residual chalcogens, as confirmed with PL, Raman, XRD, and TEM.[125] These group III nitrides are of interest for optoelectronic devices, demonstrating the technological relevance of nitride-based morphotaxy.

Another approach developed by Urbankowski *et al.* has taken advantage of the relative ease of obtaining carbide MXenes by etching the MAX compounds in HF (M = transition metal, X = carbon or nitrogen, A = group IIIA or IV element), followed by converting carbide MXenes into nitride

https://doi.org/10.1021/acsnano.2c00243
ACS Nano 2022, 16, 7144−7167

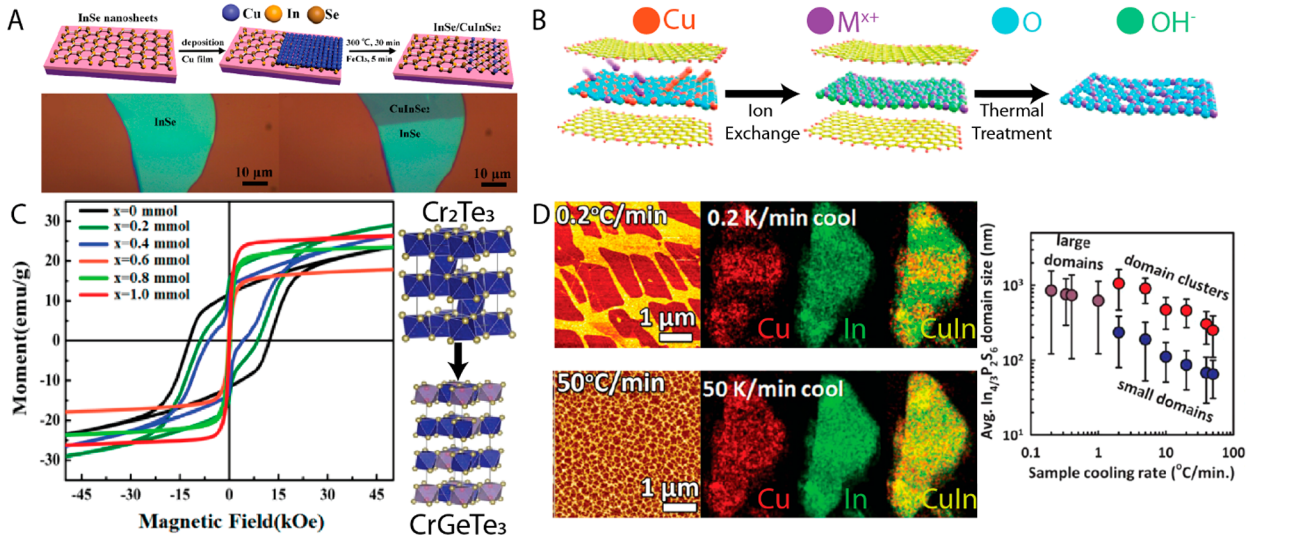

Figure 5. Cationic-based morphotaxy. (A) Synthesis schematic for lateral heterojunctions of InSe and $CuInSe_2$ formed *via* thermal treatment of InSe in the presence of evaporated Cu. The reaction proceeds only in regions where copper is thermally evaporated on top of the InSe flake, as shown in the before and after optical images. Reproduced with permission from ref 131. Copyright 2015 American Chemical Society. (B) Synthesis of ultrathin amorphous metal oxide nanosheets. By confinement of a Cu_2O template between oleate molecules and then use of an ion exchange reaction followed by a thermal treatment, ultrathin metal oxide nanosheets are synthesized in a generalizable manner (where M = Fe, Sn, Cr, Zr, Al). Adapted with permission from ref 137. Copyright 2020 American Chemical Society. (C) Synthesis of the vdW ternary compound $CrGeTe_3$ *via* cation exchange of a starting non-vdW binary compound, Cr_2Te_3. The reactants determine the magnetic behavior of the final product, with Cr_2Te_3 exhibiting hard magnetic behavior and $CrGeTe_3$ exhibiting soft magnetic behavior. Adapted with permission from ref 139. Copyright 2020 American Chemical Society. (D) Formation of a ferrielectric ($CuInP_2S_6$)–paraelectric ($In_{4/3}P_2S_6$) heterojunction *via* cationic sublattice melting. By variation of the cooling rate, the domain size of the ferrielectric and paraelectric domains can be modulated by an order of magnitude, as evidenced by phase-contrast AFM and *in situ* STEM energy-dispersive X-ray spectroscopic mapping. Adapted with permission from ref 140. Copyright 2017 American Chemical Society.

MXenes.[126] Unlike in the case of previous work on TMOs and TMDCs that adopted the hexagonal structure, the synthesized Mo_2N in this case retained the parent MXene structure while V_2N adopted a mixture of the MXene structure and the cubic VN phase. Nevertheless, the ammonized compounds demonstrated orders of magnitude increase in conductivity compared to the carbide counterparts. The stark difference in the products between Cao *et al.* and Urbankowski *et al.* emphasize the importance of the starting reactants in dictating the final product and structure when undergoing morphotaxial reactions.

Finally, recent work by Sreepal *et al.* has shown that fluorination of 2D InSe by heating exfoliated InSe flakes alongside XeF_2 crystals at 100 °C for 48 h results in the formation of InF_3 (Figure 4C).[127] Unlike previous work with carburization and nitridation of vdW materials, InF_3 is nonlayered and covalently bonded but retains the starting shape and morphology of the InSe nanosheet. Furthermore, this process has been shown to be scalable, with bulk InSe and liquid-phase exfoliated InSe also completely converted using a similar process.[127] This work demonstrates the promise of morphotaxy for achieving nonexfoliatable covalent solids in the atomically thin limit.

MORPHOTAXIAL CATIONIC MODIFICATIONS

Compared to oxidation and other anionic modifications, cationic-based morphotaxy is much less explored, due in large part to the relative difficulty of exchanging cations from a layered material. Nevertheless, a small but growing body of literature on cation exchange in layered materials is emerging to form heterojunctions or other non-vdW materials. Most of this work has focused on copper, which is a versatile cation that readily intercalates inside layered materials, although other cations have also been shown to participate in morphotaxial reactions.

Copper-Based Ion Exchange. High cationic diffusivity and comparable atomic/ionic radii are essential for cationic morphotaxy. Among possible metallic cations, copper has been the most widely explored for cationic morphotaxy, easily intercalating into the large vdW gaps found in layered materials such as Bi_2Se_3 and Bi_2Te_3. For example, Buha and Manna reported the reversible intercalation and subsequent cation exchange of copper in Bi_2Se_3.[128] By dropcasting copper nanocrystals on an amorphous carbon substrate with Bi_2Se_3 nanosheets and subsequently heating, the authors intercalated Cu into the layered material. At 250 °C and 10 atom % Cu, a superstructure was formed with the intercalated copper, whereas at 350 °C and 35 atom % Cu, the Bi_2Se_3 underwent cationic exchange to form nonlayered $Cu_{2-x}Se$. Subsequent TEM studies revealed that the resulting $Cu_{2-x}Se$ structures possessed at least 3 orientational relationships with the starting Bi_2Se_3 structure in addition to retaining the original 2D morphology, thus demonstrating successful cationic morphotaxy of $Cu_{2-x}Se$.[128] In addition, Wang *et al.* synthesized $Cu_{2-x}Se$ using CdSe as the starting material, yielding $Cu_{2-x}Se$ nanosheets as thin as 1.6 nm *via* cationic exchange with copper salt in solution.[129] Here, the CdSe starting size dictated the thickness of the product, with the thickness of the CdSe nanosheets being the same as that of the final $Cu_{2-x}Se$. The authors concluded that the anionic sublattice (Se) was preserved during cationic exchange, resulting in a cubic structure for both reactant and product.[129]

Fundamental work on studying copper intercalation and cation exchange in Bi_2Se_3 and CdSe has also helped with the

https://doi.org/10.1021/acsnano.2c00243
ACS Nano 2022, 16, 7144–7167

subsequent synthesis of heterostructures. Similar to previously discussed work, Zhan *et al.* reported the synthesis of vertical Cu_2S−CdS heterostructures *via* solution-phase cadmium to copper exchange in CdS nanosheets grown on mica.[130] The reaction occurred along the top basal plane, resulting in an atomically sharp boundary between synthesized Cu_2S and CdS or the complete conversion into Cu_2S. Photovoltaic cells using the resulting vertical Cu_2S−CdS heterojunction showed a photoelectric conversion efficiency of 2.1%, compared to a negligible photovoltaic effect in pure Cu_2S or CdS devices, which was attributed to the built-in electric field at the heterojunction.[130]

Copper-based morphotaxial formation of heterojunctions has been especially well-studied with InSe and In_2Se_3 materials since it results in optoelectronically relevant copper−indium−selenide compounds. For example, Feng *et al.* fabricated a lateral p−n heterojunction by transforming an InSe layered nanosheet into nonlayered $CuInSe_2$ by depositing Cu through thermal evaporation and subsequently heating at 300 °C for 30 min (Figure 5A).[131] Masking during the deposition of Cu resulted in atomically precise heterointerfaces between InSe and $CuInSe_2$ domains, and the resulting p−n heterostructure photodetectors showed photoresponsivities of 4.2 A W^{-1} and power conversion efficiencies of 3.5%, illustrating the benefit of morphotaxially forming p−n junctions through cation intercalation. In related work, Ji *et al.* designed a lateral $CuInSe_2$−InSe heterojunction by using PLD to deposit InSe onto a mica substrate with prepatterned copper electrodes.[132] Unlike Feng *et al.*, the authors observed lateral diffusion of Cu atoms from the electrodes during the growth of InSe due to the highly energetic PLD conditions, forming $CuInSe_2$ domains of ∼10 μm. In this case, the resulting photodetectors showed modest responsivities (0.147 mA W^{-1}) but were nevertheless notable due to their mechanical flexibility under tensile and compressive strain during bending.[132]

Similar cationic exchange has been studied with the related layered material In_2Se_3. In particular, Tao *et al.* synthesized single-crystal $CuInSe_2$ nanosheets *via* mechanically exfoliating In_2Se_3, sputtering Cu, and annealing under Ar at 350 °C for ∼1 h.[133] The researchers then used femtosecond pump−probe optical reflectivity to show that the cooling of hot carriers dominated the carrier dynamics within the first few picoseconds following optical pumping, with the detailed dynamics showing a thickness dependence.[133] Similar to the work on InSe, Zheng *et al.* grew In_2Se_3 by PLD on top of prepatterned Cu/Au contacts.[134] This structure resulted in a $CuInSe_2$−In_2Se_3 heterojunction with the Cu contact providing a copper source for morphotaxy to occur in the deposited In_2Se_3 material. Subsequent photodetector characterization revealed a high photoresponsivity of 20.1 A W^{-1}, fast response time of 8.3 ms, and broad spectral range of 370−1550 nm.[134]

Copper cation exchange can also occur in IV−VI compounds such as SnS_2. Specifically, Wang *et al.* found that the few-layer morphology of SnS_2 is preserved after a tin to copper cationic exchange, with the anionic sulfur framework inhibiting the formation of monoclinic Cu_2S and instead resulting in hexagonal Cu_2SnS_3.[135] These fundamental studies help emphasize the importance of not just the starting material composition but also the crystal structure in determining the outcome of morphotaxial synthesis.

Copper-based cationic morphotaxy is not restricted to intercalation but also applies to the dealloying of the parent structure. This approach has been used to synthesize copper-based ternary and quaternary chalcogenide nanosheets starting from CuS nanoplates, as shown by Wu *et al.*[136] The authors employed this template-mediated transformation to synthesize copper indium sulfide, copper indium gallium sulfide, and copper zinc tin sulfide by exposing CuS nanoplates to metal precursors at high temperatures (*e.g.*, indium(III) 2,4-pentanedionate was reacted at 260 °C for 2 h). Relying on structural similarities, gallium can also be inserted in place of indium by substituting In^{3+} ions with Zn^{2+} and Sn^{4+} ions. Being a 2D material, CuS thus allows for exquisite control of the morphology as well as the composition of the product, enabling the formation of inorganic multilayers for photovoltaic applications.[135] The concept of copper-based layered materials acting as a scaffold has also been explored by Jia *et al.*, who confined a Cu_2O nanosheet in an oleate shell and subsequently reacted the Cu_2O nanosheet with metal ions (Figure 5B).[137] Subsequent thermal treatment removed excess hydroxides and oleate molecules, resulting in 2D amorphous metal oxide nanosheets. This technique is generalizable to a diverse range of metal ions (Fe, Sn, Cr, Zr, Al), resulting in an extensive library of ultrathin metal oxide nanosheets. Furthermore, binary amorphous metal oxides have been synthesized, such as $SnZrO_x$.[137]

Other Cationic Exchanges. While copper participates either as the target cationic substitution or as a matrix element that is subsequently removed in most of the cationic morphotaxial demonstrations to date, a few studies have begun exploring additional cations. For instance, Baek *et al.* reported the cation-regulated transformation of ALD-grown SnS_2 into SnS by flowing Sn vapor at 240 °C.[138] Unlike previous SnS synthesis routes, which involve the decomposition of SnS_2 at high temperatures into SnS *via* desulfurization, the Sn vapor here was crucial in regulating the transformation and resulted in highly oriented, large-area films of SnS. A thin-film complementary metal-oxide-semiconductor inverter was then fabricated by selectively transforming n-type SnS_2 into SnS, demonstrating the strength of this low-temperature process in electronic devices.[138] In addition, Yang *et al.* synthesized ternary vdW $CrGeTe_3$ by reacting germanium with a non-vdW template, Cr_2Te_3 (Figure 5C).[139] Here, all of the chromium sites were replaced by germanium from a GeI_4 precursor, breaking the Cr−Te ionic bonds and introducing a vdW gap. In addition to TEM analysis, the authors confirmed this transformation through temperature-dependent measurements of the magnetization. While Cr_2Te_3 is a hard magnet, $CrGeTe_3$ is a soft magnet, and correspondingly, the coercivity changes as more Ge is added into the system and forms the soft magnetic phase.[139] Control over heating and cooling rates of the vdW layered ferrielectric $CuInP_2S_6$ with Cu deficiency also yielded heterojunctions, with slow cooling rates (0.2 °C) after heating to 300 °C resulting in large, micrometer-sized domains of paraelectric ($In_{4/3}P_2S_6$) regions within the ferrielectric $CuInP_2S_6$ (Figure 5D).[140] This phase separation occurred because the $P_2S_6^{4-}$ anion sublattice remained rigid while the Cu^+ and In^{3+} cations were mobile above 500 K, illustrating how morphotaxy can also be used to rationally design complex heterostructures *via* cationic sublattice melting.[140] Furthermore, these results emphasize how morphotaxy as a synthesis paradigm enables the realization of technologically relevant magnetic or multiferroic phenomena.

https://doi.org/10.1021/acsnano.2c00243
ACS Nano 2022, 16, 7144−7167

Table 1. Summary of Morphotaxial Synthesis Materials

starting material	ending material	processing conditions	refs
		TMDCs	
MoS_2	MoO_x	heating in air at 400 °C	72
		O_2 plasma	54,55
		oxidative-scanning probe lithography	85
	$MoSe_2$	elemental Se at 600−900 °C	105,110
	MoSSe	stripping top sulfur layer with H_2 plasma followed by selenization at 450 °C	87,117
	Mo_2C	CH_4 at 750−820 °C	121,122
	Mo_5N_6	urea at 800 °C	124
$MoSe_2$	MoO_x	remote O_2 plasma	53
	MoS_2	elemental S at 600−900 °C	104,105,109
		laser-assisted conversion using H_2S	107
	MoSSe	elemental S at 800 °C	115
		H_2 plasma assisted sulfurization with elemental S at room temperature	114,119
HfS_2	HfO_x	O_2 plasma	47,59
	HfO_2	laser illumination in air	48
$HfSe_2$	$HfSe_xO_y$	O_2 plasma	60
	HfO_2	air exposure	46
$PtSe_2$	PtSe	heating up to 550 °C in vacuum	92
	PtSSe	heating at 370−400 °C in ultrahigh vacuum to form Se vacancies, then exposing to H_2S at 350 °C	118
TaS_2	Ta_2O_5	heating in air at 300 °C	44,45
TiS_2	TiO_2	heating in air at 300 °C	44
	TiN	urea at 800 °C	124
WS_2	W_5N_6	urea at 800 °C	124
	WSSe	elemental Se at 300 °C	116
WSe_2	WO_x	air exposure	74
		O_2 plasma	54,63,86
		remote O_2 plasma	53
		ozone at 100 °C	56,57
		oxidative-scanning probe lithography	84
		heating in air at 400 °C	61
		heating in air at 50−400 °C followed by vacuum at 200 °C	62
	WO_3	heating in air at 400 °C	61,65
	WSe_yO_x	UV ozone and O_2 plasma at room temperature	64
	WS_2	laser-assisted conversion with H_2S	107
		elemental S at 700 °C	109
	WSSe	H_2 plasma assisted sulfurization with elemental S at room temperature	114,119
$ZrSe_2$	ZrO_2	air exposure	46
		TMOs	
MoO_2	MoS_2	elemental S at 850−900 °C	96
MoO_3	MoS_2	heating in H_2 at 500 °C followed by sulfurization with elemental S at 1000 °C	94
		elemental S at 750 °C	95
		heating in H_2 at 650−750 °C followed by sulfurization with H_2S at 650−850 °C	108
	MoN	NH_3 at 650−700 °C	123,125
MoO_x	MoS_2	elemental S at 300−650 °C	106
	$MoSe_2$	elemental Se at 300−650 °C	106
VO_x	V_2N	NH_3 at 800 °C	123
V_2O_5	VN	NH_3 at 500 °C	125
WO_3	WS_2	H_2 at 650−750 °C followed by H_2S at 650−850 °C	108
	WSe_2	H_2 at 750 °C followed by H_2Se at 650 °C	108
		dimethyl selenium at 600−900 °C	98
	W_2N	NH_3 at 700 °C	123
		III−VI Compounds	
GaS	GaN	NH_3 at 650 °C	125
GaSe	GaN	NH_3 at 600 °C	125
InSe	InO_x	O_2 (30 Torr) at 25 °C	68
InSe	InO_x	UV-ozone treatment at 80 °C	69
	In_2O_3	heating in air at 100−175 °C or under laser illumination	70
	InF_3	XeF_2 at 100−350 °C	127
	$CuInSe_2$	thermal evaporation of Cu followed by heating at 300 °C	131

https://doi.org/10.1021/acsnano.2c00243
ACS Nano 2022, 16, 7144−7167

Table 1. continued

starting material	ending material	processing conditions	refs
		III–VI Compounds	
		InSe is grown directly on Cu electrodes *via* PLD; Cu diffuses into InSe during deposition	132
In_2Se_3	$CuInSe_2$	sputtering of Cu followed by heating at 350 °C	133
		In_2Se_3 is grown directly on Cu electrodes *via* PLD; Cu diffuses into In_2Se_3 during deposition	134
		Other Chalcogenides	
Bi_2Se_3	$Cu_{2-x}Se$	dropcasting of Cu nanocrystals followed by heating at 250–450 °C	128
Bi_2Te_3	$Cu_{2-x}Te$	dropcasting of Cu nanocrystals followed by heating at 250–450 °C	128
	BiTeCl	$BiCl_3$ at 190 °C	120
	BiTeBr	$BiBr_3$ at 200 °C	120
Bi_2O_2Se	Bi_2SeO_5	heating in air at 370–400 °C	51
		O_2 plasma	52
Cr_2Te_3	$CrGeTe_3$	GeI_4 at 100 °C (suspension) followed by heating at 330 °C	139
CdS	Cu_2S	CuCl aqueous solution at 90 °C	130
CdSe	$Cu_{2-x}Se$	$[Cu(CH_3CN)_4]PF_6$ in methanol/toluene at room temperature	129
CuS	$CuInS_2$, $CuIn_xGa_{1-x}S_2$, Cu_2ZnSnS_4	indium(III) 2,4-pentanedionate/gallium(III) 2,4-pentanedionate/tin(IV) chloride bis(2,4-pentanedionate) in 1-dodecanethiol at 260 °C	136
SnS	SnS_2	elemental S at 227 °C	111
SnS_2	SnS	heating at 500–600 °C under argon	88,89
		heating at 300–500 °C in vacuum	91
		electron-beam irradiation at 25–400 °C	93
		dimethylamino-2-methyl-2-propoxy-tin(II) at 52 °C	138
	Cu_2SnS_3	$[Cu(CH_3CN)_4]PF_6$ in methanol at room temperature	135
$SnSe_2$	SnO_2	air exposure at room temperature	71
	SnSe	heating at 300 °C	90
		electron-beam irradiation at 25–400 °C	93
TiS_3	TiO_2	heating in air at 300 °C	58
		Black Phosphorus	
BP	PO_x	O_2 plasma	66,67
		exposure to ambient conditions (20 °C and 45% RH)	81
		tapping mode conductive AFM with Pt and Au coated tips	82
		laser oxidation	83
		Metals and Metal Oxides	
SnO_2	SnS_2	elemental S at 400 °C	99
Cu	Cu_2Se	Se deposition on Cu(111) followed by heating at 200 °C	102
Cu_2O	Fe_2O_3, Cr_2O_3, ZrO_2, SnO_2, and Al_2O_3	metal chloride salt is added to Cu_2O–oleate complex, dried in vacuum, and heated in air at 300 °C (500 °C for Fe oxide)	137
Ti	$TiSe_2$	elemental Se at 650 °C	101
Nb	$NbSe_2$	elemental Se at 600 °C	101
Pd	$PdTe_2$	elemental Te at 470 °C	103
Pt	$PtSe_2$	plasma of N_2/H_2 gas (1:1) carrying Se at 100–250 °C	100
		selenium MBE deposition followed by heating at 370 °C	118
		MXenes and MAX Structures	
various MAX structures (M = Ti, Y, Nb, Mo, Ta, W)	corresponding TMDCs	H_2S (for sulfides) or Se (for selenides) at 800–1100 °C	112
2D-Mo_2C	Mo_2N	NH_3 at 600 °C	126
2D-V_2C	V_2N and VN	NH_3 at 600 °C	126
		Miscellaneous	
$Cu_{1-x}In_{1+x/3}P_2S_6$	$CuInP_2S_6$ and $In_{4/3}P_2S_6$	phase separation at 230 °C upon cooling	140
MoS_xO_y	MoS_2	H_2S at 1000 °C	97

CONCLUSIONS AND FUTURE OUTLOOK

In this Review, we have introduced morphotaxy as a synthetic paradigm, particularly in the context of 2D materials. The number of layered 2D vdW and nonlayered 2D materials is rapidly growing, which provides a vast phase space for interconverting these materials while preserving their shape, thickness, surface smoothness, and atomically defined boundaries, as summarized in Table 1. In this final section, we highlight the most intriguing aspects of morphotaxy and focus on opportunities for future work (Figure 6).

The ultrathin nature of 2D materials coupled with substrate effects often favor the formation of unusual or metastable phases, which are challenging to achieve in bulk materials. Combined with the morphotaxial conversion approach, 2D materials, heterostructures, and device geometries become experimentally feasible for materials that normally do not exhibit single layer geometry. For example, utilizing controllable oxidation, Zhang *et al.* converted the top layer of polished

https://doi.org/10.1021/acsnano.2c00243
ACS Nano 2022, 16, 7144–7167

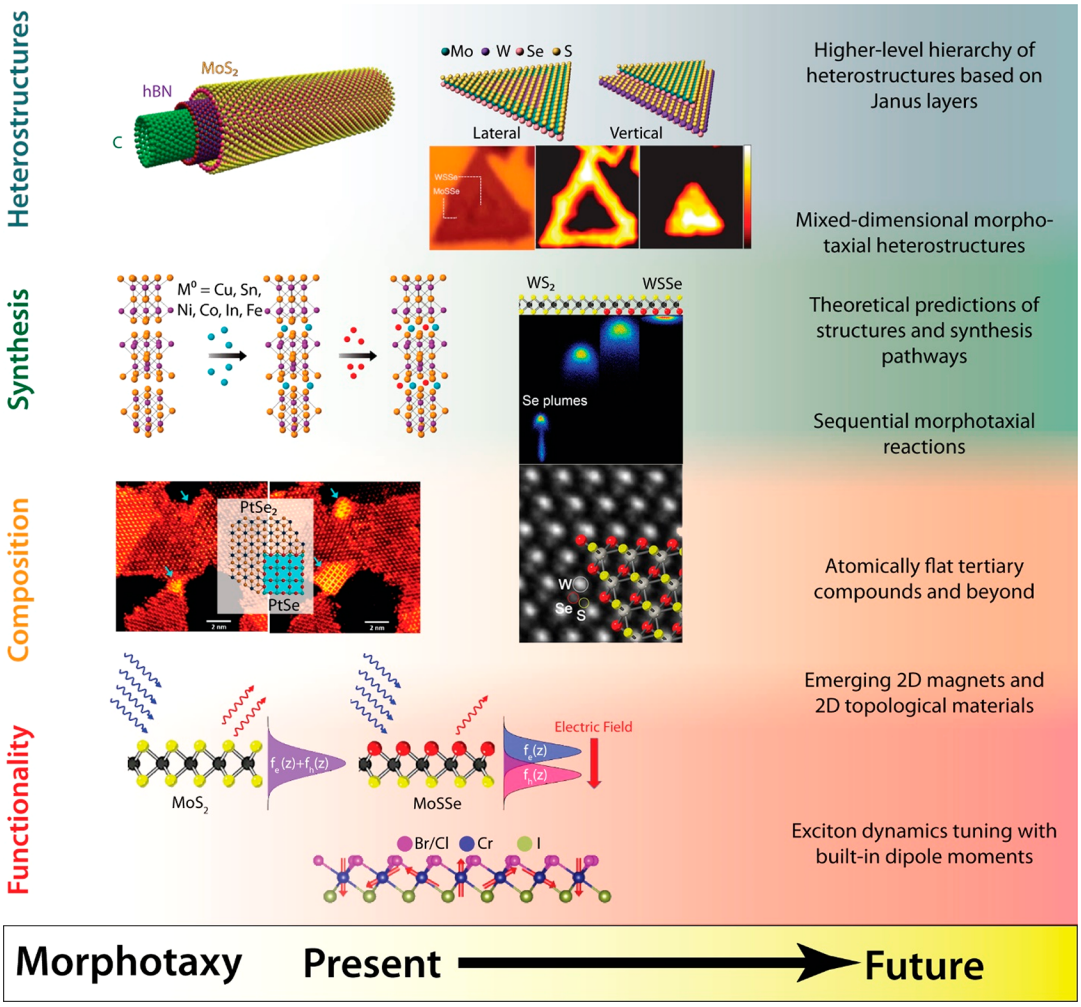

Figure 6. Future directions for morphotaxy. Heterostructures. The concept of morphotaxy facilitates the formation of lateral or vertical heterostructures. The extreme scenario enabled by morphotaxy is the formation of Janus heterostructures. Reproduced with permission from ref 114. Copyright 2020 Wiley. The concept of morphotaxy can be further extended to 1D heterostructures. Adapted with permission from ref 142. Copyright 2020 AAAS. Synthesis. Many morphotaxial synthetic methods remain to be explored such as dual cation intercalation (Adapted with permission from ref 145. Copyright 2015 American Chemical Society) and PLD plasma implantation (Adapted with permission from ref 116. Copyright 2020 American Chemical Society). Composition. Morphotaxy allows compositions that are not naturally occurring to become accessible such as PtSe (Reproduced with permission from ref 92. Copyright 2019 American Chemical Society) and Janus structures of TMDCs (Adapted with permission from ref 116. Copyright 2020 American Chemical Society). Functionality. Among the various functionalities enabled by morphotaxy, Janus structures offer properties that are not available in non-Janus materials, such as skyrmion states in monolayers of chromium halides (Adapted with permission from ref 147. Copyright 2020 American Physical Society) and exciton dynamics that are tuned by the built-in dipole moment in MoSSe (Adapted with permission from ref 146. Copyright 2021 American Chemical Society).

metal substates into metal oxides with vdW layers.[141] The subsequent transfer onto insulating substrates permitted characterization of the electronic properties of these layered metal oxides down to the monolayer limit with crystal structures distinct from the bulk oxide. Although the vast majority of morphotaxial transformations of 2D materials are performed starting from the top surface, the underlying substrate itself can also act as a platform for chemical transformations. In particular, this goal can be achieved by thermally or electrochemically driving dopants from the substrate into a surface-mounted nanosheet in order to change the composition and modify the structure. Prepatterning the substrate allows further spatial control over dopant confinement, enabling fabrication of lateral heterostructures.

One of the most promising aspects enabled by morphotaxy is the realization of complex vertical and lateral heterostructures with atomically sharp interfaces. In particular, Trivedi *et al.* extended beyond traditional heterostructure examples and prepared lateral and vertical heterostructures of Janus metal chalcogenides.[114] While the formation of lateral Janus interfaces was achieved by converting lateral MoS_2–WS_2 heterostructures into Janus MoSSe–WSSe heterostructures, the preparation of vertical stacks of Janus crystals required combining the growth with polymer-assisted flake transfer steps. As the properties of bilayers of S–Mo–Se and S–W–Se are different from bilayers of Se–Mo–S and S–W–Se or bilayers of S–Mo–Se and Se–W–S, one needs to precisely list the stacking sequence at a level of atomic planes or sublayers. This complexity creates another level of hierarchy in 2D materials heterostructures, enabled by morphotaxial preparation of Janus layers.

https://doi.org/10.1021/acsnano.2c00243
ACS Nano 2022, 16, 7144–7167

The concept of morphotaxy can also be extended beyond two dimensions. Recently, Xiang *et al.* reported the preparation of 1D vdW heterostructures of single-walled carbon nanotubes (SWCNTs) and boron nitride nanotubes (BNNTs), as well as SWCNT−BNNT−MoS_2 heterostructures *via* CVD using SWCNTs as a template for the growth.[142] Due to the p-type and n-type character of SWCNTs and MoS_2, respectively, a radial semiconductor−insulator−semiconductor heterojunction was realized in the latter case, which showed diode-like rectifying transport.[143] The concept of 1D morphotaxy can be further extended beyond SWCNTs as the growth template to nanotubes of other vdW materials. For example, Zhao *et al.* recently reported rolling of TMDC flakes and their heterostructures into nanotubes, which further broadens the number of different 1D templates for 1D morphotaxial conversions.[144]

The development of innovative synthetic approaches is enabling the realization of materials and device topologies. Recently, Lin *et al.* demonstrated the formation of Janus WSSe layers by low-energy Se implantation into WS_2.[116] This method can potentially be generalized to other TMDCs and related 2D materials. Furthermore, Chen *et al.*[145] demonstrated intercalation of multiple metal cations into Bi_2Se_3, resulting in a library of dual intercalated Bi_2Se_3 nanoribbons. Sequential intercalation has considerable potential for the fine-tuning the properties of 2D materials or devices. Since morphotaxy demonstrations thus far are dominated by metal chalcogenides, most morphotaxial transformations involve group 16 elements. However, morphotaxy provides synthetic pathways beyond oxides and chalcogenides including halides,[127] nitrides,[123,124,126] and carbides,[112] which often are nonlayered and therefore challenging to achieve in the atomically thin limit. Moving into tertiary compounds, such as oxycarbides, chalcopnictides, and chalcohalides, creates almost endless opportunities for tuning the composition of 2D materials.

In addition to expanding the compositional range of 2D materials, morphotaxial conversions also present opportunities to alter properties and thus achieve functionalities unobtainable through more traditional synthetic techniques. For example, morphotaxy has enabled the synthesis of high-κ 2D dielectrics[51,52] and 2D metals[122,124] and can be applied to achieve more exotic and emerging 2D phenomena, such as 2D magnetism and topological materials. Starting from a non-vdW Cr_2Te_3 template, Yang *et al.* synthesized $CrGeTe_3$ nanosheets and demonstrated the existence of long-range ferromagnetic order.[139] In addition, Zheng *et al.* demonstrated that the Janus structure MoSSe has a built-in out-of-plane dipole moment that leads to significantly longer radiative exciton recombination lifetimes.[146] Although experimental realization of Janus transition metal halides remains challenging, an increasing number of theoretical studies have predicted their magnetic properties.[147−152] Recently, Xu *et al.* calculated that topological spin textures (*e.g.*, helical cycloid phases, skyrmions, and bimerons) should also be achievable in Janus $Cr(I,Cl)_3$.[147] Preparation and control over such nontrivial spin textures are critical for the development of future memory devices and other emerging spintronic applications.

Although the concept of morphotaxy strongly relies on the development of experimental synthetic methods, theoretical studies will remain essential in guiding experimental efforts. As an example, the number of theoretical studies of Janus structures has rapidly grown,[147−176] which is helpful in identifying promising targets for synthesis. Theoretical studies are not only essential in describing and predicting properties but also aid in understanding the mechanisms of morphotaxial transformations (*e.g.*, defect formation, boundary propagation, and phase segregation) that can help identify and refine experimental synthetic efforts.

Inspired by many examples of experimental discoveries resulting from the principles of morphotaxial design, this Review has attempted to organize and categorize morphotaxy as a general synthetic concept. This comprehensive overview on current work in morphotaxial synthesis also provides a roadmap for leveraging morphotaxial design principles in designing next-generation materials. By expanding the scope and application of an already diverse class of materials, future work on morphotaxy will push the technological limits of low-dimensional materials by introducing complex geometries, compositions, and phenonema. In this manner, morphotaxy is likely to have broad impact on a diverse range of emerging and unanticipated fundamental studies and applied technologies.

AUTHOR INFORMATION

Corresponding Author

Mark C. Hersam − *Department of Materials Science and Engineering, Northwestern University, Evanston, Illinois 60208, United States; Department of Chemistry and Department of Electrical and Computer Engineering, Northwestern University, Evanston, Illinois 60208, United States;* orcid.org/0000-0003-4120-1426; Email: m-hersam@northwestern.edu

Authors

David Lam − *Department of Materials Science and Engineering, Northwestern University, Evanston, Illinois 60208, United States;* orcid.org/0000-0003-4264-0033

Dmitry Lebedev − *Department of Materials Science and Engineering, Northwestern University, Evanston, Illinois 60208, United States;* orcid.org/0000-0002-1866-9234

Complete contact information is available at: https://pubs.acs.org/10.1021/acsnano.2c00243

Author Contributions

The manuscript was written through contributions of all authors. All authors have given approval to the final version of the manuscript.

Notes

The authors declare no competing financial interest.

ACKNOWLEDGMENTS

David Lam acknowledges support from the Department of Energy (DOE DE-SC0019356), and Dmitry Lebedev acknowledges support from the Swiss National Science Foundation for an Early PostDoc Mobility Fellowship (P2EZP2_181614) in addition to the National Science Foundation Division of Materials Research (NSF DMR-2004420).

VOCABULARY

morphotaxy	the synthesis of low-dimensional materials by using the shape of an initial nanoscale precursor to template growth or chemical conversion

https://doi.org/10.1021/acsnano.2c00243
ACS Nano 2022, 16, 7144−7167

Janus structure	a low-dimensional material with an asymmetric two-faced structure due to atomic substitutions or functionalization on one side but not the other
van der Waals material	a material composed of atomically thin layers with strong covalent in-plane bonding and weak van der Waals interlayer bonding, which allows the material to be exfoliated *via* micromechanical or liquid phase processing
nonlayered 2D material	a solid material with a nonlayered crystal structure that is synthesized in a two-dimensional form, where the lateral size of the material far exceeds that of the thickness
heterostructure	a multilayer stack of different materials, preferably with atomically clean interfaces as is readily achieved using van der Waals materials
high-κ dielectric	materials with large dielectric constants that enable strong capacitive coupling between a gate electrode and a semiconductor channel in a field effect transistor

REFERENCES

(1) Novoselov, K. S.; Geim, A. K.; Morozov, S. V.; Jiang, D.; Zhang, Y.; Dubonos, S. V.; Grigorieva, I. V.; Firsov, A. A. Electric Field in Atomically Thin Carbon Films. *Science* **2004**, *306* (5696), 666−669.

(2) Mak, K. F.; Lee, C.; Hone, J.; Shan, J.; Heinz, T. F. Atomically Thin MoS_2: A New Direct-Gap Semiconductor. *Phys. Rev. Lett.* **2010**, *105* (13), 136805.

(3) Bandurin, D. A.; Tyurnina, A. V.; Yu, G. L.; Mishchenko, A.; Zólyomi, V.; Morozov, S. V.; Kumar, R. K.; Gorbachev, R. V.; Kudrynskyi, Z. R.; Pezzini, S.; Kovalyuk, Z. D.; Zeitler, U.; Novoselov, K. S.; Patanè, A.; Eaves, L.; Grigorieva, I. V.; Fal'Ko, V. I.; Geim, A. K.; Cao, Y. High Electron Mobility, Quantum Hall Effect and Anomalous Optical Response in Atomically Thin InSe. *Nat. Nanotechnol.* **2017**, *12* (3), 223−227.

(4) Han, J. H.; Kwak, M.; Kim, Y.; Cheon, J. Recent Advances in the Solution-Based Preparation of Two-Dimensional Layered Transition Metal Chalcogenide Nanostructures. *Chem. Rev.* **2018**, *118* (13), 6151−6188.

(5) Hernandez, Y.; Nicolosi, V.; Lotya, M.; Blighe, F. M.; Sun, Z.; De, S.; McGovern, I. T.; Holland, B.; Byrne, M.; Gun'ko, Y. K.; Boland, J. J.; Niraj, P.; Duesberg, G.; Krishnamurthy, S.; Goodhue, R.; Hutchison, J.; Scardaci, V.; Ferrari, A. C.; Coleman, J. N. High-Yield Production of Graphene by Liquid-Phase Exfoliation of Graphite. *Nat. Nanotechnol.* **2008**, *3* (9), 563−568.

(6) Coleman, J. N.; Lotya, M.; O'Neill, A.; Bergin, S. D.; King, P. J.; Khan, U.; Young, K.; Gaucher, A.; De, S.; Smith, R. J.; Shvets, I. V.; Arora, S. K.; Stanton, G.; Kim, H. Y.; Lee, K.; Kim, G. T.; Duesberg, G. S.; Hallam, T.; Boland, J. J.; Wang, J. J.; Donegan, J. F.; Grunlan, J. C.; Moriarty, G.; Shmeliov, A.; Nicholls, R. J.; Perkins, J. M.; Grieveson, E. M.; Theuwissen, K.; McComb, D. W.; Nellist, P. D.; Nicolosi, V. Two-Dimensional Nanosheets Produced by Liquid Exfoliation of Layered Materials. *Science* **2011**, *331* (6017), 568−571.

(7) Kang, J.; Wood, J. D.; Wells, S. A.; Lee, J. H.; Liu, X.; Chen, K. S.; Hersam, M. C. Solvent Exfoliation of Electronic-Grade, Two-Dimensional Black Phosphorus. *ACS Nano* **2015**, *9* (4), 3596−3604.

(8) Lam, D.; Chen, K. S.; Kang, J.; Liu, X.; Hersam, M. C. Anhydrous Liquid-Phase Exfoliation of Pristine Electrochemically Active GeS Nanosheets. *Chem. Mater.* **2018**, *30* (7), 2245−2250.

(9) Naguib, M.; Kurtoglu, M.; Presser, V.; Lu, J.; Niu, J.; Heon, M.; Hultman, L.; Gogotsi, Y.; Barsoum, M. W. Two-Dimensional Nanocrystals Produced by Exfoliation of Ti_3AlC_2. *Adv. Mater.* **2011**, *23* (37), 4248−4253.

(10) Naguib, M.; Mashtalir, O.; Carle, J.; Presser, V.; Lu, J.; Hultman, L.; Gogotsi, Y.; Barsoum, M. W. Two-Dimensional Transition Metal Carbides. *ACS Nano* **2012**, *6* (2), 1322−1331.

(11) Alhabeb, M.; Maleski, K.; Mathis, T. S.; Sarycheva, A.; Hatter, C. B.; Uzun, S.; Levitt, A.; Gogotsi, Y. Selective Etching of Silicon from Ti_3SiC_2 (MAX) To Obtain 2D Titanium Carbide (MXene). *Angew. Chemie - Int. Ed.* **2018**, *57* (19), 5444−5448.

(12) Eda, G.; Yamaguchi, H.; Voiry, D.; Fujita, T.; Chen, M.; Chhowalla, M. Photoluminescence from Chemically Exfoliated MoS_2. *Nano Lett.* **2011**, *11* (12), 5111−5116.

(13) Lin, Z.; Liu, Y.; Halim, U.; Ding, M.; Liu, Y.; Wang, Y.; Jia, C.; Chen, P.; Duan, X.; Wang, C.; Song, F.; Li, M.; Wan, C.; Huang, Y.; Duan, X. Solution-Processable 2D Semiconductors for High-Performance Large-Area Electronics. *Nature* **2018**, *562* (7726), 254−258.

(14) Backes, C.; Szydłowska, B. M.; Harvey, A.; Yuan, S.; Vega-Mayoral, V.; Davies, B. R.; Zhao, P. L.; Hanlon, D.; Santos, E. J. G.; Katsnelson, M. I.; Blau, W. J.; Gadermaier, C.; Coleman, J. N. Production of Highly Monolayer Enriched Dispersions of Liquid-Exfoliated Nanosheets by Liquid Cascade Centrifugation. *ACS Nano* **2016**, *10* (1), 1589−1601.

(15) Kang, J.; Seo, J.-W. T.; Alducin, D.; Ponce, A.; Yacaman, M. J.; Hersam, M. C. Thickness Sorting of Two-Dimensional Transition Metal Dichalcogenides via Copolymer-Assisted Density Gradient Ultracentrifugation. *Nat. Commun.* **2014**, *5*, 5478.

(16) Ahn, E.; Lee, T.; Gu, M.; Park, M.; Min, S. H.; Kim, B.-S. Layer-by-Layer Assembly for Graphene-Based Multilayer Nanocomposites: The Field Manual. *Chem. Mater.* **2017**, *29* (1), 69−79.

(17) Zhu, J.; Liu, X.; Geier, M. L.; McMorrow, J. J.; Jariwala, D.; Beck, M. E.; Huang, W.; Marks, T. J.; Hersam, M. C. Layer-by-Layer Assembled 2D Montmorillonite Dielectrics for Solution-Processed Electronics. *Adv. Mater.* **2016**, *28* (1), 63−68.

(18) Secor, E. B.; Prabhumirashi, P. L.; Puntambekar, K.; Geier, M. L.; Hersam, M. C. Inkjet Printing of High Conductivity, Flexible Graphene Patterns. *J. Phys. Chem. Lett.* **2013**, *4* (8), 1347−1351.

(19) Hyun, W. J.; Secor, E. B.; Hersam, M. C.; Frisbie, C. D.; Francis, L. F. High-Resolution Patterning of Graphene by Screen Printing with a Silicon Stencil for Highly Flexible Printed Electronics. *Adv. Mater.* **2015**, *27* (1), 109−115.

(20) Jeong, S.; Yoo, D.; Jang, J.; Kim, M.; Cheon, J. Well-Defined Colloidal 2-D Layered Transition-Metal Chalcogenide Nanocrystals via Generalized Synthetic Protocols. *J. Am. Chem. Soc.* **2012**, *134* (44), 18233−18236.

(21) Xie, J.; Zhang, H.; Li, S.; Wang, R.; Sun, X.; Zhou, M.; Zhou, J.; Lou, X. W.; Xie, Y. Defect-Rich MoS_2 Ultrathin Nanosheets with Additional Active Edge Sites for Enhanced Electrocatalytic Hydrogen Evolution. *Adv. Mater.* **2013**, *25* (40), 5807−5813.

(22) De Siena, M. C.; Creutz, S. E.; Regan, A.; Malinowski, P.; Jiang, Q.; Kluherz, K. T.; Zhu, G.; Lin, Z.; De Yoreo, J. J.; Xu, X.; Chu, J. H.; Gamelin, D. R. Two-Dimensional van der Waals Nanoplatelets with Robust Ferromagnetism. *Nano Lett.* **2020**, *20* (3), 2100−2106.

(23) Cai, Z.; Liu, B.; Zou, X.; Cheng, H. M. Chemical Vapor Deposition Growth and Applications of Two-Dimensional Materials and Their Heterostructures. *Chem. Rev.* **2018**, *118* (13), 6091−6133.

(24) Walsh, L. A.; Hinkle, C. L. Van Der Waals Epitaxy: 2D Materials and Topological Insulators. *Appl. Mater. Today* **2017**, *9*, 504−515.

(25) Sangwan, V. K.; Jariwala, D.; Kim, I. S.; Chen, K. S.; Marks, T. J.; Lauhon, L. J.; Hersam, M. C. Gate-Tunable Memristive Phenomena Mediated by Grain Boundaries in Single-Layer MoS_2. *Nat. Nanotechnol.* **2015**, *10* (5), 403−406.

(26) Sangwan, V. K.; Lee, H. S.; Bergeron, H.; Balla, I.; Beck, M. E.; Chen, K. S.; Hersam, M. C. Multi-Terminal Memtransistors from Polycrystalline Monolayer Molybdenum Disulfide. *Nature* **2018**, *554* (7693), 500−504.

https://doi.org/10.1021/acsnano.2c00243
ACS Nano 2022, 16, 7144−7167

(27) Wu, J.; Tan, C.; Tan, Z.; Liu, Y.; Yin, J.; Dang, W.; Wang, M.; Peng, H. Controlled Synthesis of High-Mobility Atomically Thin Bismuth Oxyselenide Crystals. *Nano Lett.* **2017**, *17* (5), 3021−3026.
(28) Wu, J.; Liu, Y.; Tan, Z.; Tan, C.; Yin, J.; Li, T.; Tu, T.; Peng, H. Chemical Patterning of High-Mobility Semiconducting 2D Bi_2O_2Se Crystals for Integrated Optoelectronic Devices. *Adv. Mater.* **2017**, *29* (44), 1704060.
(29) Chen, W.; Khan, U.; Feng, S.; Ding, B.; Xu, X.; Liu, B. High-Fidelity Transfer of 2D Bi_2O_2Se and Its Mechanical Properties. *Adv. Funct. Mater.* **2020**, *30* (43), 2004960.
(30) Wu, W.; De, D.; Chang, S.-C.; Wang, Y.; Peng, H.; Bao, J.; Pei, S.-S. High Mobility and High on/off Ratio Field-Effect Transistors Based on Chemical Vapor Deposited Single-Crystal MoS_2 Grains. *Appl. Phys. Lett.* **2013**, *102* (14), 142106.
(31) Zhang, W.; Huang, J.-K.; Chen, C.-H.; Chang, Y.-H.; Cheng, Y.-J.; Li, L.-J. High-Gain Phototransistors Based on a CVD MoS_2 Monolayer. *Adv. Mater.* **2013**, *25* (25), 3456−3461.
(32) Yao, J. D.; Zheng, Z. Q.; Yang, G. W. Production of Large-Area 2D Materials for High-Performance Photodetectors by Pulsed-Laser Deposition. *Prog. Mater. Sci.* **2019**, *106*, 100573.
(33) Bergeron, H.; Guiney, L. M.; Beck, M. E.; Zhang, C.; Sangwan, V. K.; Torres-Castanedo, C. G.; Gish, J. T.; Rao, R.; Austin, D. R.; Guo, S.; Lam, D.; Su, K.; Brown, P. T.; Glavin, N. R.; Maruyama, B.; Bedzyk, M. J.; Dravid, V. P.; Hersam, M. C. Large-Area Optoelectronic-Grade InSe Thin Films via Controlled Phase Evolution. *Appl. Phys. Rev.* **2020**, *7* (4), 041402.
(34) Muratore, C.; Voevodin, A. A.; Glavin, N. R. Physical Vapor Deposition of 2D Van Der Waals Materials: A Review. *Thin Solid Films* **2019**, *688*, 137500.
(35) Mannix, A. J.; Zhou, X. F.; Kiraly, B.; Wood, J. D.; Alducin, D.; Myers, B. D.; Liu, X.; Fisher, B. L.; Santiago, U.; Guest, J. R.; Yacaman, M. J.; Ponce, A.; Oganov, A. R.; Hersam, M. C.; Guisinger, N. P. Synthesis of Borophenes: Anisotropic, Two-Dimensional Boron Polymorphs. *Science* **2015**, *350* (6267), 1513−1516.
(36) Mannix, A. J.; Kiraly, B.; Fisher, B. L.; Hersam, M. C.; Guisinger, N. P. Silicon Growth at the Two-Dimensional Limit on Ag(111). *ACS Nano* **2014**, *8* (7), 7538−7547.
(37) Mannix, A. J.; Kiraly, B.; Hersam, M. C.; Guisinger, N. P. Synthesis and Chemistry of Elemental 2D Materials. *Nat. Rev. Chem.* **2017**, *1*, 0014.
(38) Fu, D.; Zhao, X.; Zhang, Y. Y.; Li, L.; Xu, H.; Jang, A. R.; Yoon, S. I.; Song, P.; Poh, S. M.; Ren, T.; Ding, Z.; Fu, W.; Shin, T. J.; Shin, H. S.; Pantelides, S. T.; Zhou, W.; Loh, K. P. Molecular Beam Epitaxy of Highly Crystalline Monolayer Molybdenum Disulfide on Hexagonal Boron Nitride. *J. Am. Chem. Soc.* **2017**, *139* (27), 9392−9400.
(39) Park, J.; Mitchel, W. C.; Grazulis, L.; Smith, H. E.; Eyink, K. G.; Boeckl, J. J.; Tomich, D. H.; Pacley, S. D.; Hoelscher, J. E. Epitaxial Graphene Growth by Carbon Molecular Beam Epitaxy (CMBE). *Adv. Mater.* **2010**, *22* (37), 4140−4145.
(40) Shannon, R. D.; Rossi, R. C. Definition of Topotaxy. *Nature* **1964**, *202* (4936), 1000−1001.
(41) Illarionov, Y. Y.; Knobloch, T.; Jech, M.; Lanza, M.; Akinwande, D.; Vexler, M. I.; Mueller, T.; Lemme, M. C.; Fiori, G.; Schwierz, F.; Grasser, T. Insulators for 2D Nanoelectronics: The Gap to Bridge. *Nat. Commun.* **2020**, *11*, 3385.
(42) Kang, J.; Wells, S. A.; Sangwan, V. K.; Lam, D.; Liu, X.; Luxa, J.; Sofer, Z.; Hersam, M. C. Solution-Based Processing of Optoelectronically Active Indium Selenide. *Adv. Mater.* **2018**, *30* (38), 1802990.
(43) Gish, J. T.; Lebedev, D.; Stanev, T. K.; Jiang, S.; Georgopoulos, L.; Song, T. W.; Lim, G.; Garvey, E. S.; Valdman, L.; Balogun, O.; Sofer, Z.; Sangwan, V. K.; Stern, N. P.; Hersam, M. C. Ambient-Stable Two-Dimensional CrI_3 via Organic-Inorganic Encapsulation. *ACS Nano* **2021**, *15* (6), 10659−10667.
(44) Cui, Q.; Sakhdari, M.; Chamlagain, B.; Chuang, H. J.; Liu, Y.; Cheng, M. M. C.; Zhou, Z.; Chen, P. Y. Ultrathin and Atomically Flat Transition-Metal Oxide: Promising Building Blocks for Metal-Insulator Electronics. *ACS Appl. Mater. Interfaces* **2016**, *8* (50), 34552−34558.
(45) Chamlagain, B.; Cui, Q.; Paudel, S.; Cheng, M. M.-C.; Chen, P.-Y.; Zhou, Z. Thermally Oxidized 2D TaS_2 as a High- κ Gate Dielectric for MoS_2 Field-Effect Transistors. *2D Mater.* **2017**, *4* (3), 031002.
(46) Mleczko, M. J.; Zhang, C.; Lee, H. R.; Kuo, H.-H.; Magyari-Köpe, B.; Moore, R. G.; Shen, Z.-X.; Fisher, I. R.; Nishi, Y.; Pop, E. $HfSe_2$ and $ZrSe_2$: Two-Dimensional Semiconductors with Native High-κ Oxides. *Sci. Adv.* **2017**, *3* (8), No. e1700481.
(47) Lai, S.; Byeon, S.; Jang, S. K.; Lee, J.; Lee, B. H.; Park, J. H.; Kim, Y. H.; Lee, S. HfO_2/HfS_2 Hybrid Heterostructure Fabricated: Via Controllable Chemical Conversion of Two-Dimensional HfS2. *Nanoscale* **2018**, *10* (39), 18758−18766.
(48) Peimyoo, N.; Barnes, M. D.; Mehew, J. D.; De Sanctis, A.; Amit, I.; Escolar, J.; Anastasiou, K.; Rooney, A. P.; Haigh, S. J.; Russo, S.; Craciun, M. F.; Withers, F. Laser-Writable High-k Dielectric for van der Waals Nanoelectronics. *Sci. Adv.* **2019**, *5* (1), No. eaau0906.
(49) Bergeron, H.; Lebedev, D.; Hersam, M. C. Polymorphism in Post-Dichalcogenide Two-Dimensional Materials. *Chem. Rev.* **2021**, *121* (4), 2713−2775.
(50) Zhang, L.; Yang, Z.; Gong, T.; Pan, R.; Wang, H.; Guo, Z.; Zhang, H.; Fu, X. High Electron Mobility and Quantum Oscillations in Non-Encapsulated Ultrathin Semiconducting $Bi2_2O_2Se$. *J. Mater. Chem. A* **2020**, *8* (18), 8813−8830.
(51) Li, T.; Tu, T.; Sun, Y.; Fu, H.; Yu, J.; Xing, L.; Wang, Z.; Wang, H.; Jia, R.; Wu, J.; Tan, C.; Liang, Y.; Zhang, Y.; Zhang, C.; Dai, Y.; Qiu, C.; Li, M.; Huang, R.; Jiao, L.; Lai, K.; Yan, B.; Gao, P.; Peng, H. A Native Oxide High-κ Gate Dielectric for Two-Dimensional Electronics. *Nat. Electron.* **2020**, *3* (8), 473−478.
(52) Tu, T.; Zhang, Y.; Li, T.; Yu, J.; Liu, L.; Wu, J.; Tan, C.; Tang, J.; Liang, Y.; Zhang, C.; Dai, Y.; Han, Y.; Lai, K.; Peng, H. Uniform High-k Amorphous Native Oxide Synthesized by Oxygen Plasma for Top-Gated Transistors. *Nano Lett.* **2020**, *20* (10), 7469−7475.
(53) Li, Z.; Yang, S.; Dhall, R.; Kosmowska, E.; Shi, H.; Chatzakis, I.; Cronin, S. B. Layer Control of WSe_2 via Selective Surface Layer Oxidation. *ACS Nano* **2016**, *10* (7), 6836−6842.
(54) Pei, C.; Li, X.; Fan, H.; Wang, J.; You, H.; Yang, P.; Wei, C.; Wang, S.; Shen, X.; Li, H. Morphological and Spectroscopic Characterizations of Monolayer and Few-Layer MoS_2 and WSe_2 Nanosheets under Oxygen Plasma Treatment with Different Excitation Power: Implications for Modulating Electronic Properties. *ACS Appl. Nano Mater.* **2020**, *3* (5), 4218−4230.
(55) Ko, T. Y.; Jeong, A.; Kim, W.; Lee, J.; Kim, Y.; Lee, J. E.; Ryu, G. H.; Park, K.; Kim, D.; Lee, Z.; Lee, M. H.; Lee, C.; Ryu, S. On-Stack Two-Dimensional Conversion of MoS_2 into MoO_3. *2D Mater.* **2017**, *4* (1), 014003.
(56) Yamamoto, M.; Nakaharai, S.; Ueno, K.; Tsukagoshi, K. Self-Limiting Oxides on WSe_2 as Controlled Surface Acceptors and Low-Resistance Hole Contacts. *Nano Lett.* **2016**, *16* (4), 2720−2727.
(57) Yamamoto, M.; Ueno, K.; Tsukagoshi, K. Pronounced Photogating Effect in Atomically Thin WSe_2 with a Self-Limiting Surface Oxide Layer. *Appl. Phys. Lett.* **2018**, *112* (18), 181902.
(58) Ghasemi, F.; Frisenda, R.; Flores, E.; Papadopoulos, N.; Biele, R.; Perez de Lara, D.; van der Zant, H. S. J.; Watanabe, K.; Taniguchi, T.; D'Agosta, R.; Ares, J. R.; Sánchez, C.; Ferrer, I. J.; Castellanos-Gomez, A. Tunable Photodetectors via In Situ Thermal Conversion of TiS_3 to TiO_2. *Nanomaterials* **2020**, *10* (4), 711.
(59) Jin, T.; Zheng, Y.; Gao, J.; Wang, Y.; Li, E.; Chen, H.; Pan, X.; Lin, M.; Chen, W. Controlling Native Oxidation of HfS_2 for 2D Materials Based Flash Memory and Artificial Synapse. *ACS Appl. Mater. Interfaces* **2021**, *13* (8), 10639−10649.
(60) Liu, L.; Li, Y.; Huang, X.; Chen, J.; Yang, Z.; Xue, K.; Xu, M.; Chen, H.; Zhou, P.; Miao, X. Low-Power Memristive Logic Device Enabled by Controllable Oxidation of 2D $HfSe_2$ for In-Memory Computing. *Adv. Sci.* **2021**, *8* (15), 2005038.
(61) Liu, Y.; Tan, C.; Chou, H.; Nayak, A.; Wu, D.; Ghosh, R.; Chang, H. Y.; Hao, Y.; Wang, X.; Kim, J. S.; Piner, R.; Ruoff, R. S.; Akinwande, D.; Lai, K. Thermal Oxidation of WSe_2 Nanosheets Adhered on SiO_2/Si Substrates. *Nano Lett.* **2015**, *15* (8), 4979−4984.

https://doi.org/10.1021/acsnano.2c00243
ACS Nano 2022, 16, 7144−7167

(62) Liu, B.; Ma, Y.; Zhang, A.; Chen, L.; Abbas, A. N.; Liu, Y.; Shen, C.; Wan, H.; Zhou, C. High-Performance WSe_2 Field-Effect Transistors via Controlled Formation of In-Plane Heterojunctions. *ACS Nano* **2016**, *10* (5), 5153−5160.
(63) Hoffman, A. N.; Stanford, M. G.; Sales, M. G.; Zhang, C.; Ivanov, I. N.; McDonnell, S. J.; Mandrus, D. G.; Rack, P. D. Tuning the Electrical Properties of WSe_2 via O_2 Plasma Oxidation: Towards Lateral Homojunctions. *2D Mater.* **2019**, *6* (4), 045024.
(64) Lin, Y. C.; Bersch, B. M.; Addou, R.; Xu, K.; Wang, Q.; Smyth, C. M.; Jariwala, B.; Walker, R. C.; Fullerton-Shirey, S. K.; Kim, M. J.; Wallace, R. M.; Robinson, J. A. Modification of the Electronic Transport in Atomically Thin WSe_2 by Oxidation. *Adv. Mater. Interfaces* **2020**, *7* (18), 2000422.
(65) He, H. K.; Yang, R.; Huang, H. M.; Yang, F. F.; Wu, Y. Z.; Shaibo, J.; Guo, X. Multi-Gate Memristive Synapses Realized with the Lateral Heterostructure of 2D WSe_2 and WO_3. *Nanoscale* **2020**, *12* (1), 380−387.
(66) Pei, J.; Gai, X.; Yang, J.; Wang, X.; Yu, Z.; Choi, D.-Y.; Luther-Davies, B.; Lu, Y. Producing Air-Stable Monolayers of Phosphorene and Their Defect Engineering. *Nat. Commun.* **2016**, *7* (1), 10450.
(67) Dickerson, W.; Tayari, V.; Fakih, I.; Korinek, A.; Caporali, M.; Serrano-Ruiz, M.; Peruzzini, M.; Heun, S.; Botton, G. A.; Szkopek, T. Phosphorus Oxide Gate Dielectric for Black Phosphorus Field Effect Transistors. *Appl. Phys. Lett.* **2018**, *112* (17), 173101.
(68) Ho, P. H.; Chang, Y. R.; Chu, Y. C.; Li, M. K.; Tsai, C. A.; Wang, W. H.; Ho, C. H.; Chen, C. W.; Chiu, P. W. High-Mobility InSe Transistors: The Role of Surface Oxides. *ACS Nano* **2017**, *11* (7), 7362−7370.
(69) Chen, Y.-H.; Cheng, C.-Y.; Chen, S.-Y.; Rodriguez, J. S. D.; Liao, H.-T.; Watanabe, K.; Taniguchi, T.; Chen, C.-W.; Sankar, R.; Chou, F.-C.; Chiu, H.-C.; Wang, W.-H. Oxidized-Monolayer Tunneling Barrier for Strong Fermi-Level Depinning in Layered InSe Transistors. *npj 2D Mater. Appl.* **2019**, *3*, 49.
(70) Balakrishnan, N.; Kudrynskyi, Z. R.; Smith, E. F.; Fay, M. W.; Makarovsky, O.; Kovalyuk, Z. D.; Eaves, L.; Beton, P. H.; Patanè, A. Engineering p - n Junctions and Bandgap Tuning of InSe Nanolayers by Controlled Oxidation. *2D Mater.* **2017**, *4* (2), 025043.
(71) Paolucci, V.; D'Olimpio, G.; Kuo, C. N.; Lue, C. S.; Boukhvalov, D. W.; Cantalini, C.; Politano, A. Self-Assembled $SnO_2/SnSe_2$ Heterostructures: A Suitable Platform for Ultrasensitive NO_2 and H_2 Sensing. *ACS Appl. Mater. Interfaces* **2020**, *12* (30), 34362−34369.
(72) Yoon, A.; Kim, J. H.; Yoon, J.; Lee, Y.; Lee, Z. Van Der Waals Epitaxial Formation of Atomic Layered α-MoO_3 on MoS_2 by Oxidation. *ACS Appl. Mater. Interfaces* **2020**, *12* (19), 22029−22036.
(73) Das, S. R.; Wakabayashi, K.; Tsukagoshi, K.; Dutta, S. Ab-Initio Investigation of Preferential Triangular Self-Formation of Oxide Heterostructures of Monolayer WSe_2. *Sci. Rep.* **2020**, *10*, 21737.
(74) Xu, H.; Han, X.; Liu, W.; Liu, P.; Fang, H.; Li, X.; Li, Z.; Guo, J.; Xiang, B.; Hu, W.; Parkin, I. P.; Wu, J.; Guo, Z.; Liu, H. Ambipolar and Robust WSe_2 Field-Effect Transistors Utilizing Self-Assembled Edge Oxides. *Adv. Mater. Interfaces* **2020**, *7* (1), 1901628.
(75) Longo, R. C.; Addou, R.; KC, S.; Noh, J.-Y.; Smyth, C. M.; Barrera, D.; Zhang, C.; Hsu, J. W. P.; Wallace, R. M.; Cho, K. Intrinsic Air Stability Mechanisms of Two-Dimensional Transition Metal Dichalcogenide Surfaces: Basal versus Edge Oxidation. *2D Mater.* **2017**, *4* (2), 025050.
(76) Gronborg, S. S.; Thorarinsdottir, K.; Kyhl, L.; Rodriguez-Fernández, J.; Sanders, C. E.; Bianchi, M.; Hofmann, P.; Miwa, J. A.; Ulstrup, S.; Lauritsen, J. V. Basal Plane Oxygen Exchange of Epitaxial MoS_2 without Edge Oxidation. *2D Mater.* **2019**, *6* (4), 045013.
(77) Park, J. H.; Vishwanath, S.; Liu, X.; Zhou, H.; Eichfeld, S. M.; Fullerton-Shirey, S. K.; Robinson, J. A.; Feenstra, R. M.; Furdyna, J.; Jena, D.; Xing, H. G.; Kummel, A. C. Scanning Tunneling Microscopy and Spectroscopy of Air Exposure Effects on Molecular Beam Epitaxy Grown WSe_2 Monolayers and Bilayers. *ACS Nano* **2016**, *10* (4), 4258−4267.
(78) Addou, R.; Smyth, C. M.; Noh, J.-Y.; Lin, Y.-C.; Pan, Y.; Eichfeld, S. M.; Fölsch, S.; Robinson, J. A.; Cho, K.; Feenstra, R. M.; Wallace, R. M. One Dimensional Metallic Edges in Atomically Thin WSe_2 Induced by Air Exposure. *2D Mater.* **2018**, *5* (2), 025017.
(79) Ziletti, A.; Carvalho, A.; Trevisanutto, P. E.; Campbell, D. K.; Coker, D. F.; Castro Neto, A. H. Phosphorene Oxides: Bandgap Engineering of Phosphorene by Oxidation. *Phys. Rev. B* **2015**, *91* (8), 085407.
(80) Kuntz, K. L.; Wells, R. A.; Hu, J.; Yang, T.; Dong, B.; Guo, H.; Woomer, A. H.; Druffel, D. L.; Alabanza, A.; Tománek, D.; Warren, S. C. Control of Surface and Edge Oxidation on Phosphorene. *ACS Appl. Mater. Interfaces* **2017**, *9* (10), 9126−9135.
(81) Robbins, M. C.; Namgung, S.; Oh, S. H.; Koester, S. J. Cyclical Thinning of Black Phosphorus with High Spatial Resolution for Heterostructure Devices. *ACS Appl. Mater. Interfaces* **2017**, *9* (14), 12654−12662.
(82) Liu, X.; Chen, K.; Wells, S. A.; Balla, I.; Zhu, J.; Wood, J. D.; Hersam, M. C. Scanning Probe Nanopatterning and Layer-by-Layer Thinning of Black Phosphorus. *Adv. Mater.* **2017**, *29*, 1604121.
(83) Lu, J.; Wu, J.; Carvalho, A.; Ziletti, A.; Liu, H.; Tan, J.; Chen, Y.; Castro Neto, A. H.; Özyilmaz, B.; Sow, C. H. Bandgap Engineering of Phosphorene by Laser Oxidation toward Functional 2D Materials. *ACS Nano* **2015**, *9* (10), 10411−10421.
(84) Dago, A. I.; Ryu, Y. K.; Palomares, F. J.; Garcia, R. Direct Patterning of p-Type-Doped Few-Layer WSe_2 Nanoelectronic Devices by Oxidation Scanning Probe Lithography. *ACS Appl. Mater. Interfaces* **2018**, *10* (46), 40054−40061.
(85) Ryu, Y. K.; Dago, A. I.; He, Y.; Espinosa, F. M.; López-Elvira, E.; Munuera, C.; Garcia, R. Sub-10 Nm Patterning of Few-Layer MoS_2 and $MoSe_2$ Nanolectronic Devices by Oxidation Scanning Probe Lithography. *Appl. Surf. Sci.* **2021**, *539*, 148231.
(86) Mitta, S. B.; Ali, F.; Yang, Z.; Moon, I.; Ahmed, F.; Yoo, T. J.; Lee, B. H.; Yoo, W. J. Gate-Modulated Ultrasensitive Visible and Near-Infrared Photodetection of Oxygen Plasma-Treated WSe_2 Lateral pn-Homojunctions. *ACS Appl. Mater. Interfaces* **2020**, *12* (20), 23261−23271.
(87) Lu, A. Y.; Zhu, H.; Xiao, J.; Chuu, C. P.; Han, Y.; Chiu, M. H.; Cheng, C. C.; Yang, C. W.; Wei, K. H.; Yang, Y.; Wang, Y.; Sokaras, D.; Nordlund, D.; Yang, P.; Muller, D. A.; Chou, M. Y.; Zhang, X.; Li, L. J. Janus Monolayers of Transition Metal Dichalcogenides. *Nat. Nanotechnol.* **2017**, *12* (8), 744−749.
(88) Jiang, Y.; Ding, Y.; Chen, F.; Wang, Z.; Xu, Y.; Huang, S.; Chen, Z.; Zhao, B.; Zhang, J. Structural Phase Transformation from SnS_2/Reduced Graphene Oxide to SnS/Sulfur-Doped Graphene and Its Lithium Storage Properties. *Nanoscale* **2020**, *12* (3), 1697−1706.
(89) Zhou, T.; Pang, W. K.; Zhang, C.; Yang, J.; Chen, Z.; Liu, H. K.; Guo, Z. Enhanced Sodium-Ion Battery Performance by Structural Phase Transition from Two-Dimensional Hexagonal-SnS_2 to Orthorhombic-SnS. *ACS Nano* **2014**, *8* (8), 8323−8333.
(90) Tian, Z.; Zhao, M.; Xue, X.; Xia, W.; Guo, C.; Guo, Y.; Feng, Y.; Xue, J. Lateral Heterostructures Formed by Thermally Converting n-Type $SnSe_2$ to p-Type SnSe. *ACS Appl. Mater. Interfaces* **2018**, *10* (15), 12831−12838.
(91) Voznyi, A.; Kosyak, V.; Grase, L.; Vecstaudža, J.; Onufrijevs, P.; Yeromenko, Y.; Medvid', A.; Opanasyuk, A. Formation of SnS Phase Obtained by Thermal Vacuum Annealing of SnS_2 Thin Films and Its Application in Solar Cells. *Mater. Sci. Semicond. Process.* **2018**, *79*, 32−39.
(92) Ryu, G. H.; Chen, J.; Wen, Y.; Warner, J. H. In-Situ Atomic-Scale Dynamics of Thermally Driven Phase Transition of 2D Few-Layered 1T $PtSe_2$ into Ultrathin 2D Nonlayered PtSe Crystals. *Chem. Mater.* **2019**, *31* (23), 9895−9903.
(93) Sutter, E.; Huang, Y.; Komsa, H. P.; Ghorbani-Asl, M.; Krasheninnikov, A. V.; Sutter, P. Electron-Beam Induced Transformations of Layered Tin Dichalcogenides. *Nano Lett.* **2016**, *16* (7), 4410−4416.
(94) Lin, Y. C.; Zhang, W.; Huang, J. K.; Liu, K. K.; Lee, Y. H.; Liang, C. Te; Chu, C. W.; Li, L. J. Wafer-Scale MoS_2 Thin Layers Prepared by MoO_3 Sulfurization. *Nanoscale* **2012**, *4* (20), 6637−6641.

https://doi.org/10.1021/acsnano.2c00243
ACS Nano 2022, 16, 7144−7167

(95) Taheri, P.; Wang, J.; Xing, H.; Destino, J. F.; Arik, M. M.; Zhao, C.; Kang, K.; Blizzard, B.; Zhang, L.; Zhao, P.; Huang, S.; Yang, S.; Bright, F. V.; Cerne, J.; Zeng, H. Growth Mechanism of Largescale MoS_2 Monolayer by Sulfurization of MoO_3 Film. *Mater. Res. Express* **2016**, *3* (7), 075009.
(96) Wang, X.; Feng, H.; Wu, Y.; Jiao, L. Controlled Synthesis of Highly Crystalline MoS_2 Flakes by Chemical Vapor Deposition. *J. Am. Chem. Soc.* **2013**, *135* (14), 5304−5307.
(97) Sohn, A.; Kim, C.; Jung, J.; Kim, J. H.; Byun, K.; Cho, Y.; Zhao, P.; Kim, S. W.; Seol, M.; Lee, Z.; Kim, S.; Shin, H. Precise Layer Control and Electronic State Modulation of a Transition Metal Dichalcogenide via Phase-Transition-Induced Growth. *Adv. Mater.* **2021**, 2103286.
(98) Browning, P.; Eichfeld, S.; Zhang, K.; Hossain, L.; Lin, Y. C.; Wang, K.; Lu, N.; Waite, A. R.; Voevodin, A. A.; Kim, M.; Robinson, J. A. Large-Area Synthesis of WSe_2 from WO_3 by Selenium-Oxygen Ion Exchange. *2D Mater.* **2015**, *2*, 014003.
(99) Yang, X.; Xiao, F.; Wang, S.; Liu, J.; Leung, M. K. H.; Yu, D. Y. W.; Rogach, A. L. Confined Annealing-Induced Transformation of Tin Oxide into Sulfide for Sodium Storage Applications. *J. Mater. Chem. A* **2019**, *7* (19), 11877−11885.
(100) Su, T.-Y.; Medina, H.; Chen, Y.-Z.; Wang, S.-W.; Lee, S.-S.; Shih, Y.-C.; Chen, C.-W.; Kuo, H.-C.; Chuang, F.-C.; Chueh, Y.-L. Phase-Engineered $PtSe_2$-Layered Films by a Plasma-Assisted Selenization Process toward All $PtSe_2$-Based Field Effect Transistor to Highly Sensitive, Flexible, and Wide-Spectrum Photoresponse Photodetectors. *Small* **2018**, *14* (19), 1800032.
(101) Lin, H.; Zhu, Q.; Shu, D.; Lin, D.; Xu, J.; Huang, X.; Shi, W.; Xi, X.; Wang, J.; Gao, L. Growth of Environmentally Stable Transition Metal Selenide Films. *Nat. Mater.* **2019**, *18* (6), 602−607.
(102) Yang, Y.; Wu, Q.; Deng, J.; Wang, J.; Xia, Y.; Fu, X.; Tian, Q.; Zhang, L.; Yin, L.-J.; Tian, Y.; Xie, S.-Y.; Zhang, L.; Qin, Z. Realization of Semiconducting Cu_2Se by Direct Selenization of Cu(111). *Chinese Phys. B* **2021**, *30* (11), 116802.
(103) Zheng, J.; Miao, T.; Xu, R.; Ping, X.; Wu, Y.; Lu, Z.; Zhang, Z.; Hu, D.; Liu, L.; Zhang, Q.; Li, D.; Cheng, Z.; Ma, W.; Xie, L.; Jiao, L. Chemical Synthesis and Integration of Highly Conductive $PdTe_2$ with Low-Dimensional Semiconductors for P-Type Transistors with Low Contact Barriers. *Adv. Mater.* **2021**, *33* (27), 2101150.
(104) Ghosh, R.; Kim, J. S.; Roy, A.; Chou, H.; Vu, M.; Banerjee, S. K.; Akinwande, D. Large Area Chemical Vapor Deposition Growth of Monolayer $MoSe_2$ and Its Controlled Sulfurization to MoS_2. *J. Mater. Res.* **2016**, *31* (7), 917−922.
(105) Su, S. H.; Hsu, W. T.; Hsu, C. L.; Chen, C. H.; Chiu, M. H.; Lin, Y. C.; Chang, W. H.; Suenaga, K.; He, J. H.; Li, L. J. Controllable Synthesis of Band-Gap-Tunable and Monolayer Transition-Metal Dichalcogenide Alloys. *Front. Energy Res.* **2014**, *2*, 27.
(106) Sadler, E. C.; Kempa, T. J. Chalcogen Incorporation Process during High-Vacuum Conversion of Bulk Mo Oxides to Mo Dichalcogenides. *ACS Appl. Electron. Mater.* **2020**, *2* (4), 1020−1025.
(107) Afaneh, T.; Sahoo, P. K.; Nobrega, I. A. P.; Xin, Y.; Gutiérrez, H. R. Laser-Assisted Chemical Modification of Monolayer Transition Metal Dichalcogenides. *Adv. Funct. Mater.* **2018**, *28* (37), 1802949.
(108) Kemelbay, A.; Kuntubek, A.; Chang, N.; Chen, C. T.; Kastl, C.; Inglezakis, V. J.; Tikhonov, A.; Schwartzberg, A. M.; Aloni, S.; Kuykendall, T. R. Lithographically Defined Synthesis of Transition Metal Dichalcogenides. *2D Mater.* **2019**, *6* (4), 045055.
(109) Mahjouri-Samani, M.; Lin, M.-W.; Wang, K.; Lupini, A. R.; Lee, J.; Basile, L.; Boulesbaa, A.; Rouleau, C. M.; Puretzky, A. A.; Ivanov, I. N.; Xiao, K.; Yoon, M.; Geohegan, D. B. Patterned Arrays of Lateral Heterojunctions within Monolayer Two-Dimensional Semiconductors. *Nat. Commun.* **2015**, *6*, 7749.
(110) Li, H.; Wu, X.; Liu, H.; Zheng, B.; Zhang, Q.; Zhu, X.; Wei, Z.; Zhuang, X.; Zhou, H.; Tang, W.; Duan, X.; Pan, A. Composition-Modulated Two-Dimensional Semiconductor Lateral Heterostructures via Layer-Selected Atomic Substitution. *ACS Nano* **2017**, *11* (1), 961−967.
(111) Li, S.; Wang, Y.; Cheng, P.; Feng, B.; Chen, L.; Wu, K. Realization of Large Scale, 2D van der Waals Heterojunction of SnS_2/SnS by Reversible Sulfurization. *Small* **2021**, *17* (37), 2101154.
(112) Du, Z.; Yang, S.; Li, S.; Lou, J.; Zhang, S.; Wang, S.; Li, B.; Gong, Y.; Song, L.; Zou, X.; Ajayan, P. M. Conversion of Non-van der Waals Solids to 2D Transition-Metal Chalcogenides. *Nature* **2020**, *577* (7791), 492−496.
(113) Zhang, L.; Yang, Z.; Gong, T.; Pan, R.; Wang, H.; Guo, Z.; Zhang, H.; Fu, X. Recent Advances in Emerging Janus Two-Dimensional Materials: From Fundamental Physics to Device Applications. *J. Mater. Chem. A* **2020**, *8* (18), 8813−8830.
(114) Trivedi, D. B.; Turgut, G.; Qin, Y.; Sayyad, M. Y.; Hajra, D.; Howell, M.; Liu, L.; Yang, S.; Patoary, N. H.; Li, H.; Petrić, M. M.; Meyer, M.; Kremser, M.; Barbone, M.; Soavi, G.; Stier, A. V.; Müller, K.; Yang, S.; Esqueda, I. S.; Zhuang, H.; Finley, J. J.; Tongay, S. Room-Temperature Synthesis of 2D Janus Crystals and Their Heterostructures. *Adv. Mater.* **2020**, *32* (50), 2006320.
(115) Zhang, J.; Jia, S.; Kholmanov, I.; Dong, L.; Er, D.; Chen, W.; Guo, H.; Jin, Z.; Shenoy, V. B.; Shi, L.; Lou, J. Janus Monolayer Transition-Metal Dichalcogenides. *ACS Nano* **2017**, *11* (8), 8192−8198.
(116) Lin, Y. C.; Liu, C.; Yu, Y.; Zarkadoula, E.; Yoon, M.; Puretzky, A. A.; Liang, L.; Kong, X.; Gu, Y.; Strasser, A.; Meyer, H. M.; Lorenz, M.; Chisholm, M. F.; Ivanov, I. N.; Rouleau, C. M.; Duscher, G.; Xiao, K.; Geohegan, D. B. Low Energy Implantation into Transition-Metal Dichalcogenide Monolayers to Form Janus Structures. *ACS Nano* **2020**, *14* (4), 3896−3906.
(117) Zhang, K.; Guo, Y.; Ji, Q.; Lu, A. Y.; Su, C.; Wang, H.; Puretzky, A. A.; Geohegan, D. B.; Qian, X.; Fang, S.; Kaxiras, E.; Kong, J.; Huang, S. Enhancement of van der Waals Interlayer Coupling through Polar Janus MoSSe. *J. Am. Chem. Soc.* **2020**, *142* (41), 17499−17507.
(118) Sant, R.; Gay, M.; Marty, A.; Lisi, S.; Harrabi, R.; Vergnaud, C.; Dau, M. T.; Weng, X.; Coraux, J.; Gauthier, N.; Renault, O.; Renaud, G.; Jamet, M. Synthesis of Epitaxial Monolayer Janus SPtSe. *npj 2D Mater. Appl.* **2020**, *4*, 41.
(119) Petrić, M. M.; Kremser, M.; Barbone, M.; Qin, Y.; Sayyad, Y.; Shen, Y.; Tongay, S.; Finley, J. J.; Botello-Méndez, A. R.; Müller, K. Raman Spectrum of Janus Transition Metal Dichalcogenide Monolayers WSSe and MoSSe. *Phys. Rev. B* **2021**, *103* (3), 035414.
(120) Hajra, D.; Sailus, R.; Blei, M.; Yumigeta, K.; Shen, Y.; Tongay, S. Epitaxial Synthesis of Highly Oriented 2D Janus Rashba Semiconductor BiTeCl and BiTeBr Layers. *ACS Nano* **2020**, *14* (11), 15626−15632.
(121) Zhao, Z.; Qin, F.; Kasiraju, S.; Xie, L.; Alam, M. K.; Chen, S.; Wang, D.; Ren, Z.; Wang, Z.; Grabow, L. C.; Bao, J. Vertically Aligned MoS_2/Mo_2C Hybrid Nanosheets Grown on Carbon Paper for Efficient Electrocatalytic Hydrogen Evolution. *ACS Catal.* **2017**, *7* (10), 7312−7318.
(122) Jeon, J.; Park, Y.; Choi, S.; Lee, J.; Lim, S. S.; Lee, B. H.; Song, Y. J.; Cho, J. H.; Jang, Y. H.; Lee, S. Epitaxial Synthesis of Molybdenum Carbide and Formation of a Mo_2C/MoS_2 Hybrid Structure via Chemical Conversion of Molybdenum Disulfide. *ACS Nano* **2018**, *12* (1), 338−346.
(123) Xiao, X.; Yu, H.; Jin, H.; Wu, M.; Fang, Y.; Sun, J.; Hu, Z.; Li, T.; Wu, J.; Huang, L.; Gogotsi, Y.; Zhou, J. Salt-Templated Synthesis of 2D Metallic MoN and Other Nitrides. *ACS Nano* **2017**, *11* (2), 2180−2186.
(124) Cao, J.; Li, T.; Gao, H.; Lin, Y.; Wang, X.; Wang, H.; Palacios, T.; Ling, X. Realization of 2D Crystalline Metal Nitrides via Selective Atomic Substitution. *Sci. Adv.* **2020**, *6* (2), No. eaax8784.
(125) Sreedhara, M. B.; Vasu, K.; Rao, C. N. R. Synthesis and Characterization of Few-Layer Nanosheets of GaN and Other Metal Nitrides. *Zeitschrift fur Anorg. und Allg. Chemie* **2014**, *640* (14), 2737−2741.
(126) Urbankowski, P.; Anasori, B.; Hantanasirisakul, K.; Yang, L.; Zhang, L.; Haines, B.; May, S. J.; Billinge, S. J. L.; Gogotsi, Y. 2D Molybdenum and Vanadium Nitrides Synthesized by Ammoniation of

https://doi.org/10.1021/acsnano.2c00243
ACS Nano 2022, 16, 7144−7167

2D Transition Metal Carbides (MXenes). *Nanoscale* **2017**, *9* (45), 17722−17730.
(127) Sreepal, V.; Yagmurcukardes, M.; Vasu, K. S.; Kelly, D. J.; Taylor, S. F. R.; Kravets, V. G.; Kudrynskyi, Z.; Kovalyuk, Z. D.; Patanè, A.; Grigorenko, A. N.; Haigh, S. J.; Hardacre, C.; Eaves, L.; Sahin, H.; Geim, A. K.; Peeters, F. M.; Nair, R. R. Two-Dimensional Covalent Crystals by Chemical Conversion of Thin van der Waals Materials. *Nano Lett.* **2019**, *19* (9), 6475−6481.
(128) Buha, J.; Manna, L. Solid State Intercalation, Deintercalation, and Cation Exchange in Colloidal 2D Bi_2Se_3 and Bi_2Te_3 Nanocrystals. *Chem. Mater.* **2017**, *29* (3), 1419−1429.
(129) Wang, Y.; Zhukovskyi, M.; Tongying, P.; Tian, Y.; Kuno, M. Synthesis of Ultrathin and Thickness-Controlled $Cu_{2-x}Se$ Nanosheets via Cation Exchange. *J. Phys. Chem. Lett.* **2014**, *5* (21), 3608−3613.
(130) Zhan, Y.; Shao, Z.; Jiang, T.; Ye, J.; Wu, X.; Zhang, B.; Ding, K.; Wu, D.; Jie, J. Cation Exchange Synthesis of Two-Dimensional Vertical Cu_2S/CdS Heterojunctions for Photovoltaic Device Applications. *J. Mater. Chem. A* **2020**, *8* (2), 789−796.
(131) Feng, W.; Zheng, W.; Chen, X.; Liu, G.; Cao, W.; Hu, P. Solid-State Reaction Synthesis of a InSe/$CuInSe_2$ Lateral p-n Heterojunction and Application in High Performance Optoelectronic Devices. *Chem. Mater.* **2015**, *27* (3), 983−989.
(132) Ji, H.; Xie, M.; Zhou, J.; Wang, X.; Jin, Z.; Jiang, K.; Shang, L.; Hu, Z.; Chu, J. Self-Assembly of a Lateral Quasi-Ohmic $CuInSe_2$/InSe Isotype Heterojunction for Flexible Devices by Pulsed Laser Deposition. *Appl. Phys. Lett.* **2019**, *115* (16), 162104.
(133) Tao, X.; Mafi, E.; Gu, Y. Synthesis and Ultrafast Carrier Dynamics of Single-Crystal Two-Dimensional $CuInSe_2$ Nanosheets. *J. Phys. Chem. Lett.* **2014**, *5* (16), 2857−2862.
(134) Zheng, Z.; Yao, J.; Yang, G. Self-Assembly of the Lateral In_2Se_3/$CuInSe_2$ Heterojunction for Enhanced Photodetection. *ACS Appl. Mater. Interfaces* **2017**, *9* (8), 7288−7296.
(135) Wang, Y.; Morozov, Y. V.; Zhukovskyi, M.; Chatterjee, R.; Draguta, S.; Tongying, P.; Bryant, B.; Rouvimov, S.; Kuno, M. Transforming Layered to Nonlayered Two-Dimensional Materials: Cation Exchange of SnS_2 to Cu_2SnS_3. *ACS Energy Lett.* **2016**, *1* (1), 175−181.
(136) Wu, X. J.; Huang, X.; Qi, X.; Li, H.; Li, B.; Zhang, H. Copper-Based Ternary and Quaternary Semiconductor Nanoplates: Templated Synthesis, Characterization, and Photoelectrochemical Properties. *Angew. Chemie - Int. Ed.* **2014**, *53* (34), 8929−8933.
(137) Jia, B.; Yang, J.; Hao, R.; Li, L.; Guo, L. Confined Synthesis of Ultrathin Amorphous Metal-Oxide Nanosheets. *ACS Mater. Lett.* **2020**, *2* (6), 610−615.
(138) Baek, I. H.; Pyeon, J. J.; Lee, G. Y.; Song, Y. G.; Lee, H.; Won, S. O.; Han, J. H.; Kang, C. Y.; Chung, T. M.; Hwang, C. S.; Kim, S. K. Cation-Regulated Transformation for Continuous Two-Dimensional Tin Monosulfide. *Chem. Mater.* **2020**, *32* (6), 2313−2320.
(139) Yang, H.; Wang, F.; Zhang, H.; Guo, L.; Hu, L.; Wang, L.; Xue, D. J.; Xu, X. Solution Synthesis of Layered van der Waals (VdW) Ferromagnetic $CrGeTe_3$ Nanosheets from a Non-VdW Cr_2Te_3 Template. *J. Am. Chem. Soc.* **2020**, *142* (9), 4438−4444.
(140) Susner, M. A.; Chyasnavichyus, M.; Puretzky, A. A.; He, Q.; Conner, B. S.; Ren, Y.; Cullen, D. A.; Ganesh, P.; Shin, D.; Demir, H.; McMurray, J. W.; Borisevich, A. Y.; Maksymovych, P.; McGuire, M. A. Cation-Eutectic Transition via Sublattice Melting in $CuInP_2S_6$/$In_{4/3}P_2S_6$ van der Waals Layered Crystals. *ACS Nano* **2017**, *11* (7), 7060−7073.
(141) Zhang, B. Y.; Xu, K.; Yao, Q.; Jannat, A.; Ren, G.; Field, M. R.; Wen, X.; Zhou, C.; Zavabeti, A.; Ou, J. Z. Hexagonal Metal Oxide Monolayers Derived from the Metal-Gas Interface. *Nat. Mater.* **2021**, *20* (8), 1073−1078.
(142) Xiang, R.; Inoue, T.; Zheng, Y.; Kumamoto, A.; Qian, Y.; Sato, Y.; Liu, M.; Tang, D.; Gokhale, D.; Guo, J.; Hisama, K.; Yotsumoto, S.; Ogamoto, T.; Arai, H.; Kobayashi, Y.; Zhang, H.; Hou, B.; Anisimov, A.; Maruyama, M.; Miyata, Y.; Okada, S.; Chiashi, S.; Li, Y.; Kong, J.; Kauppinen, E. I.; Ikuhara, Y.; Suenaga, K.; Maruyama, S. One-Dimensional van der Waals Heterostructures. *Science* **2020**, *367* (6477), 537−542.
(143) Feng, Y.; Li, H.; Inoue, T.; Chiashi, S.; Rotkin, S. V.; Xiang, R.; Maruyama, S. One-Dimensional van der Waals Heterojunction Diode. *ACS Nano* **2021**, *15* (3), 5600−5609.
(144) Zhao, B.; Wan, Z.; Liu, Y.; Xu, J.; Yang, X.; Shen, D.; Zhang, Z.; Guo, C.; Qian, Q.; Li, J.; Wu, R.; Lin, Z.; Yan, X.; Li, B.; Zhang, Z.; Ma, H.; Li, B.; Chen, X.; Qiao, Y.; Shakir, I.; Almutairi, Z.; Wei, F.; Zhang, Y.; Pan, X.; Huang, Y.; Ping, Y.; Duan, X.; Duan, X. High-Order Superlattices by Rolling up van der Waals Heterostructures. *Nature* **2021**, *591* (7850), 385−390.
(145) Chen, K. P.; Chung, F. R.; Wang, M.; Koski, K. J. Dual Element Intercalation into 2D Layered Bi_2Se_3 Nanoribbons. *J. Am. Chem. Soc.* **2015**, *137* (16), 5431−5437.
(146) Zheng, T.; Lin, Y.-C.; Yu, Y.; Valencia-Acuna, P.; Puretzky, A. A.; Torsi, R.; Liu, C.; Ivanov, I. N.; Duscher, G.; Geohegan, D. B.; Ni, Z.; Xiao, K.; Zhao, H. Excitonic Dynamics in Janus MoSSe and WSSe Monolayers. *Nano Lett.* **2021**, *21* (2), 931−937.
(147) Xu, C.; Feng, J.; Prokhorenko, S.; Nahas, Y.; Xiang, H.; Bellaiche, L. Topological Spin Texture in Janus Monolayers of the Chromium Trihalides $Cr(I,X)_3$. *Phys. Rev. B* **2020**, *101* (6), 060404.
(148) Wang, Y.; Wei, W.; Wang, H.; Mao, N.; Li, F.; Huang, B.; Dai, Y. Janus TiXY Monolayers with Tunable Berry Curvature. *J. Phys. Chem. Lett.* **2019**, *10* (23), 7426−7432.
(149) Zhang, F.; Zhang, H.; Mi, W.; Wang, X. Electronic Structure, Magnetic Anisotropy and Dzyaloshinskii-Moriya Interaction in Janus $Cr_2I_3X_3$(X = Br, Cl) Bilayers. *Phys. Chem. Chem. Phys.* **2020**, *22* (16), 8647−8657.
(150) Ren, Y.; Li, Q.; Wan, W.; Liu, Y.; Ge, Y. High-Temperature Ferromagnetic Semiconductors: Janus Monolayer Vanadium Trihalides. *Phys. Rev. B* **2020**, *101* (13), 134421.
(151) Guan, Z.; Luo, N.; Ni, S.; Hu, S. Tunable Electronic and Magnetic Properties of Monolayer and Bilayer Janus $Cr_2Cl_3I_3$: A First-Principles Study. *Mater. Adv.* **2020**, *1* (2), 244−253.
(152) Zhang, Z.; You, J. Y.; Gu, B.; Su, G. Antiferromagnetic and Electric Polarized States in Two-Dimensional Janus Semiconductor $Fe_2Cl_3I_3$. *J. Phys. Chem. C* **2020**, *124* (35), 19219−19227.
(153) Zhang, C.; Nie, Y.; Sanvito, S.; Du, A. First-Principles Prediction of a Room-Temperature Ferromagnetic Janus VSSe Monolayer with Piezoelectricity, Ferroelasticity, and Large Valley Polarization. *Nano Lett.* **2019**, *19* (2), 1366−1370.
(154) Zhao, H.; Xie, F.; Liu, Y.; Bian, B.; Yang, G.; Ding, Y.; Gu, Y.; Yu, Y.; Zhang, X.; Huo, X.; Hua, B.; Ni, X.; Fan, Q.; Gu, X. Van Der Waals Heterostructures of Janus XSeTe (X = Mo, W) and Arsenene Monolayers: A First Principles Study. *Mater. Sci. Semicond. Process.* **2021**, *123*, 105588.
(155) Pham, T. H.; Ullah, H.; Shafique, A.; Kim, H. J.; Shin, Y.-H. Enhanced Out-of-Plane Electromechanical Response of Janus ZrSeO. *Phys. Chem. Chem. Phys.* **2021**, *23* (30), 16289−16295.
(156) Wang, T.; Su, M.; Jin, H.; Li, J.; Wan, L.; Wei, Y. Optical, Electronic, and Contact Properties of Janus-MoSO/MoS_2 Heterojunction. *J. Phys. Chem. C* **2020**, *124* (29), 15988−15994.
(157) Liu, M.-Y.; Gong, L.; He, Y.; Cao, C. Tuning Rashba Effect, Band Inversion, and Spin-Charge Conversion of Janus X Sn_2 Y Monolayers via an External Field. *Phys. Rev. B* **2021**, *103* (7), 075421.
(158) Yeh, C. H. Computational Study of Janus Transition Metal Dichalcogenide Monolayers for Acetone Gas Sensing. *ACS Omega* **2020**, *5* (48), 31398−31406.
(159) She, X. C.; Zhang, R. L.; Zhao, J.; Qi, D. X.; Zou, Y.; Peng, R. Tunable Valley Polarization in Janus WSSe by Magnetic Proximity Coupling to a CrI_3: Layer. *Phys. Chem. Chem. Phys.* **2021**, *23* (33), 18182−18188.
(160) Xiong, F.; Chen, Y. A First-Principles Study of Janus Monolayer TiSSe and VSSe as Anode Materials in Alkali Metal Ion Batteries. *Nanotechnology* **2021**, *32* (2), 025702.
(161) Guo, J.; Wu, S.; Zhong, S.; Zhang, G.; Shen, G.; Yu, X. Janus WSSe Monolayer Adsorbed with Transition-Metal Atoms (Fe, Co and Ni): Excellent Performance for Gas Sensing and CO Catalytic Oxidation. *Appl. Surf. Sci.* **2021**, *565*, 150558.
(162) Guan, Z.; Ni, S.; Hu, S. Tunable Electronic and Optical Properties of Monolayer and Multilayer Janus MoSSe as a

https://doi.org/10.1021/acsnano.2c00243
ACS Nano 2022, 16, 7144−7167

Photocatalyst for Solar Water Splitting: A First-Principles Study. *J. Phys. Chem. C* **2018**, *122* (11), 6209−6216.
(163) Varjovi, M. J.; Yagmurcukardes, M.; Peeters, F. M.; Durgun, E. Janus Two-Dimensional Transition Metal Dichalcogenide Oxides: First-Principles Investigation of WXO Monolayers with X = S, Se, and Te. *Phys. Rev. B* **2021**, *103* (19), 195438.
(164) Xiao, W. Z.; Xu, L.; Xiao, G.; Wang, L. L.; Dai, X. Y. Two-Dimensional Hexagonal Chromium Chalco-Halides with Large Vertical Piezoelectricity, High-Temperature Ferromagnetism, and High Magnetic Anisotropy. *Phys. Chem. Chem. Phys.* **2020**, *22* (26), 14503−14513.
(165) Hu, Y.; Li, T.; Liu, L.; Tan, Y.; Hu, L.; Wu, K.; Yang, C. Janus XM-GaS (M = Si, Ge, Sn; X = N, P) Monolayers: Multifunctional Properties for Photocatalysis, Piezoelectricity and Second Harmonic Generation. *Phys. B Condens. Matter* **2020**, *594*, 412366.
(166) Do, T. N.; Nguyen, C. V.; Idrees, M.; Amin, B.; Tam, H. A.; Hieu, N. N.; Phuc, H. V.; Hoa, L. T. Strain Engineering of the Electro-Optical and Photocatalytic Properties of Single-Layered Janus MoSSe: First Principles Calculations. *Optik* **2020**, *224*, 165503.
(167) Cui, Z.; Bai, K.; Ding, Y.; Wang, X.; Li, E.; Zheng, J. Janus XSSe/SiC (X = Mo, W) van der Waals Heterostructures as Promising Water-Splitting Photocatalysts. *Phys. E Low-Dimensional Syst. Nanostructures* **2020**, *123*, 114207.
(168) Guan, Z.; Ni, S. Predicted 2D Ferromagnetic Janus VSeTe Monolayer with High Curie Temperature, Large Valley Polarization and Magnetic Crystal Anisotropy. *Nanoscale* **2020**, *12* (44), 22735−22742.
(169) Wang, P.; Zong, Y.; Liu, H.; Wen, H.; Deng, H. X.; Wei, Z.; Wu, H. B.; Xia, J. B. Quasiparticle Band Structure and Optical Properties of the Janus Monolayer and Bilayer SnSSe. *J. Phys. Chem. C* **2020**, *124* (43), 23832−23838.
(170) He, J.; Li, S. Two-Dimensional Janus Transition-Metal Dichalcogenides with Intrinsic Ferromagnetism and Half-Metallicity. *Comput. Mater. Sci.* **2018**, *152*, 151−157.
(171) Zhou, X.; Sun, X.; Zhang, Z.; Guo, W. Ferromagnetism in a Semiconducting Janus NbSe Hydride Monolayer. *J. Mater. Chem. C* **2018**, *6* (36), 9675−9681.
(172) Liu, J.; Ren, J.-C.; Shen, T.; Liu, X.; Butch, C. J.; Li, S.; Liu, W. Asymmetric Schottky Contacts in van der Waals Metal-Semiconductor-Metal Structures Based on Two-Dimensional Janus Materials. *Research* **2020**, *2020*, 6727524.
(173) Ding, Y.; Yang, G.; Gu, Y.; Yu, Y.; Zhang, X.; Tang, X.; Lu, N.; Wang, Y.; Dai, Z.; Zhao, H.; Li, Y. First-Principles Predictions of Janus MoSSe and WSSe for FET Applications. *J. Phys. Chem. C* **2020**, *124* (38), 21197−21206.
(174) Cui, Z.; Lyu, N.; Ding, Y.; Bai, K. Noncovalently Functionalization of Janus MoSSe Monolayer with Organic Molecules. *Phys. E Low-Dimensional Syst. Nanostructures* **2021**, *127*, 114503.
(175) Panigrahi, P.; Jini, D.; Bae, H.; Lee, H.; Ahuja, R.; Hussain, T. Two-Dimensional Janus Monolayers of MoSSe as Promising Sensor towards Selected Adulterants Compounds. *Appl. Surf. Sci.* **2021**, *542*, 148590.
(176) Zhao, Y.-M.; Ren, P.; Ma, X.-Y.; Lewis, J. P.; Yan, Q.-B.; Su, G. Effects of Vacancy and Ti Doping in 2D Janus MoSSe on Photocatalysis. *J. Phys. Chem. C* **2021**, *125* (22), 11939−11949.

https://doi.org/10.1021/acsnano.2c00243
ACS Nano 2022, 16, 7144−7167